

Accretion from a Shock-Inflated Companion: Spinning Down Neutron Stars to Hour-Long Periods

SAVANNAH CARY,¹ WENBIN LU,^{1,2} CALVIN LEUNG,¹ AND TIN LONG SUNNY WONG³

¹*Department of Astronomy, University of California, Berkeley, CA 94720-3411, USA*

²*Theoretical Astrophysics Center, University of California, Berkeley, CA 94720-3411, USA*

³*Department of Physics, University of California, Santa Barbara, CA 93106, USA*

(Received July 14, 2025)

Submitted to ApJ

ABSTRACT

Recent observations have unveiled a population of pulsars with spin periods of a few minutes to hours that lie beyond the traditional “death line.” If they originate from neutron stars (NSs), the existence of such ultra-long period pulsars (ULPs) challenges our current understanding of NS evolution and emission. In this work, we propose a new channel for disk formation based on NSs born in close binaries with main-sequence companion stars. Using a hydrodynamic simulation of supernova-companion interactions, we show that a newborn NS may gravitationally capture gas as it moves through the complex density field shaped by the explosion. For a binary separation of 20 R_{\odot} and a companion mass of 4 M_{\odot} , we find the occurrence fraction for disk formation around unbound NSs to be $\sim 10\%$. By modeling the disk evolution and its interaction with the NS, we find a bimodal distribution in spin periods: canonical pulsars with $P \lesssim 10$ s are the ones who lack disks or whose magnetospheres never interacted with the disk, and ULPs with $10^3 \lesssim P < 10^5$ s are produced when the system undergoes a short-lived “propeller” phase during which the NS undergoes rapid spin-down. Such ULPs are formed under strong initial dipolar magnetic field strengths $B_0 \gtrsim 10^{14}$ G, with a formation rate of 10^{-4} yr^{-1} in the Milky Way. We also find that a small population of pulsars with moderate magnetic field strengths ($10^{13} \lesssim B_0 \lesssim 10^{14}$ G) and relatively slow initial periods ($P_0 \gtrsim 0.1$ s) evolve to $P \sim 10^2$ s, filling the gap between the bimodal distribution. Thus, our model provides a unified explanation for pulsars beyond the “death line.”

Keywords: Pulsars (1306) — Radio transient sources (2008) — Stellar accretion disks (1579) — Binary stars (154)

1. INTRODUCTION

Prior to the past few years, radio pulsars as neutron stars (NSs) were known to have periods of $\sim 0.002\text{--}12$ s (V. M. Kaspi & A. M. Beloborodov 2017; R. N. Manchester et al. 2005, <http://www.atnf.csiro.au/research/pulsar/psrcat>). The lack of periods >12 s has been historically referred to as the “death line”: a traditional pulsar that spins down due to magnetic field decay would stop producing radio emission at these long periods, as it would no longer be able to produce electron-positron pairs along the open field lines anchored on the

polar caps ⁴(e.g., K. Chen & M. Ruderman 1993; B. Zhang et al. 2000).

The first few peculiar pulsars that pushed this upper limit included PSR J0250+5854 with a period of 23.5 s (C. M. Tan et al. 2018), PSR J1903+0433 with a period of 14 s (J. L. Han et al. 2021), and PSR J0901-4046 with a period of 76 s (M. Caleb et al. 2022). Driven by these discoveries, the death line and various aspects of the long-term evolution of NSs have been reevaluated, including magnetic field decay, inclination angle evolution, and possible influences by a fall-back accretion disk (e.g., A. P. Igoshev & S. B. Popov 2018; F. F. Kou et al.

Corresponding author: Savannah Cary
scary@berkeley.edu

⁴ Observational biases in traditional pulsar searching also play some role in the lack of long period pulsars (e.g., P. Lazarus et al. 2015; E. van Heerden et al. 2017).

2019; M. Ronchi et al. 2022; A. A. Gençali et al. 2023; X. Zhou et al. 2024).

More recently, the story has become increasingly difficult to interpret with the discovery of even slower radio pulsators whose periods do not immediately suggest NSs. These discoveries include CHIME J0630+25 (F. A. Dong et al. 2024), GLEAM-X J162759.5-523504.3 (GLEAM-J1627, N. Hurley-Walker et al. 2022), GPM 1839-10 (GMP-1839, N. Hurley-Walker et al. 2023), ASKAP J1935+2148 (ASKAP-J1935, M. Caleb et al. 2024), and ASKAP/DART J1832-0911 (ASKAP/DART-J1832, D. Li et al. 2024; Z. Wang et al. 2024), with periods of 421 s, 18.18 min, 21 min, 54 min, and 44 min, respectively. Table 1 lists these observed pulsators and their properties. Most of these sources lack precise localizations for multi-wavelength counterpart searches. An exception is ASKAP/DART-J1832, whose spatial coincidence with the supernova remnant⁵ G22.7-0.2 and radio polarization properties suggest a NS origin (D. Li et al. 2024); this is also supported by the pulsed X-ray emission during an outburst with phase-averaged luminosities of $L_X \sim 10^{33} \text{ erg s}^{-1}$ (Z. Wang et al. 2024).

Another motivation for the NS nature of some of these long-period sources is the magnetar candidate IE 161348-5055 (IE-1613), who is embedded in a young supernova remnant (SNR) RCW103 and has a rotational period of 6.7 hr (A. De Luca et al. 2006). Although IE-1613 has not been detected in the radio so far, other magnetars show transient radio emission likely powered by magnetic energy rather than rotational energy (e.g., F. Camilo et al. 2006; L. Levin et al. 2010; G. L. Israel et al. 2021; W. Zhu et al. 2023).

However, two other long-period radio pulsators, GLEAM-X J0704-37 with a 2.9 hr period and ILT J1101+5521 with a 2.1 hr period (N. Hurley-Walker et al. 2024; I. de Ruiter et al. 2024), have been detected with optical counterparts and are more likely to originate from binary systems with an M-dwarf (MD) orbiting around a white dwarf (WD). Indeed, spectroscopic measurements of GLEAM-X J0704-37 by A. C. Rodriguez (2025) confirmed the MD-WD binary nature of this source and showed that the period of radio pulsations corresponds to the orbital period. In this scenario, the radio emission is likely powered by magnetospheric interactions between a strongly magnetized WD and the MD companion (J. I. Katz 2022; A. Loeb & D. Maoz 2022; Y. Qu & B. Zhang 2024). This is analogous to the systems of AR Scorpii and J1912-4410 (T. R. Marsh

et al. 2016; B. Marcote et al. 2017; I. Pelisoli et al. 2023), although in these two well-studied systems the WD’s rotation is not synchronous with the orbit (likely due to accretion spin-up episodes).

Though this may suggest a WD-MD origin for these recently discovered long-period pulsators, many of the sources without optical counterparts (to deep limits) seem to be isolated. To date, no isolated magnetic WD has been observed to show radio pulsations. In fact, P. Beniamini et al. (2023) argued that *isolated* magnetic WDs are inconsistent with observations of these long-period sources. On one hand, WDs have very low magnetic dipole spin-down powers, L_{sd} . If we take a typical WD radius of $R_{\text{WD}} \sim 5 \times 10^3 \text{ km}$, then the spin-down power is $L_{\text{sd}} \sim 5 \times 10^{27} \text{ erg s}^{-1} (B/10^9 \text{ G})^2 (P/\text{hr})^{-4}$ for surface magnetic field strength B and spin period P . In the dipole spin-down picture, the peak luminosities of the observed radio pulses ($L \gtrsim 10^{31} \text{ erg s}^{-1}$) would generally require magnetic fields that are much stronger ($B \gg 10^9 \text{ G}$) than the most strongly magnetized WDs known (F. A. Dong et al. 2024; M. Caleb et al. 2024). On the other hand, powering the radio emission by magnetic field decay is also problematic, because the magnetic energy budget $E_B \sim 10^{43} (B/10^9 \text{ G})^2 \text{ erg}$, combined with the requirement of a cooling age of $\tau \gtrsim 10^8 \text{ yr}$ (as constrained by the optical upper limits), would give a rather low luminosity $L_B \sim E_B/\tau \lesssim 3 \times 10^{27} \text{ erg s}^{-1} (B/10^9 \text{ G})^2 (\tau/10^8 \text{ yr})^{-1}$. Therefore, if these sources are isolated, observations favor the picture of a strongly magnetized NS or magnetar where the radio pulses are magnetically powered (instead of rotationally powered).

For the purpose of this paper, we will call the sources showing radio pulsations with periods $P \gtrsim 10^3$ seconds *ultra long-period pulsars* (ULPs). We assume that a fraction of ULPs are isolated NSs, despite that no ULP (besides IE-1613) has yet been associated with a NS so far. Since NSs are generally born rapidly spinning (e.g., S. B. Popov & R. Turolla 2012; A. Noutsos et al. 2013), we focus on how to slow down an isolated NS’s spin to these ultra long periods.

A widely studied mechanism is the braking torque from an accretion disk — for strong NS magnetic fields and low accretion rates, the interactions between the accretion flow and the NS magnetosphere may slow down the spin of the NS (K. Davidson & J. P. Ostriker 1973). Spin down from accretion disks has indeed been observed in the high-mass X-ray binary system 4U 1954+319, which contains a NS with a spin period of 5.4 hrs and a red supergiant companion star of mass $\gtrsim 7 M_\odot$ (T. Enoto et al. 2014; K. H. Hinkle et al. 2020). In fact, the companion star may go supernova and be

⁵ Z. Wang et al. (2024) cautiously noted the non-negligible probability of chance coincidence.

kicked from the system, leaving behind an isolated, slow-spinning NS (Y.-H. Mao et al. 2025).

There is also observational evidence of NSs with disk accretion in their evolutionary history. One such example is pulsar PSR1257+12, who has two Earth-like planets that orbit it (A. Wolszczan & D. A. Frail 1992). Additionally, the magnetars 4U 0142+61 and 1E 2259+586 show near-infrared (NIR) emission that is likely from a debris disk heated by the NS’s X-ray emission (R. Perna et al. 2000; F. Hulleman et al. 2004; Z. Wang et al. 2006; Ü. Ertan et al. 2007; D. L. Kaplan et al. 2009), although J. Hare et al. (2024) argued for a magnetospheric origin based on the large amplitude variability of the NIR/optical emission. Furthermore, the magnetar candidate IE 1613 (with a 6.7 hr spin period) went into an outburst phase with a NIR counterpart that may be produced by an X-ray heated debris disk (S. P. Tendulkar et al. 2017; P. Esposito et al. 2019).

Previous studies on disk-magnetosphere interactions have shown that a NS can be slowed down to minute to hour long periods by an accretion disk of initial mass $M_d \sim 10^{-6} - 10^{-3} M_\odot$ (with initial magnetic field strengths in the range $\sim 10^{12} - 10^{15}$ G, e.g., A. A. Gençali et al. 2023; M. Ronchi et al. 2022; Y.-N. Fan et al. 2024; H. Tong 2023). In this framework, A. De Luca et al. (2006) and H. Tong et al. (2016) showed that IE-1613’s spin period of 6.7 hrs could be achieved with an initial disk mass of $\sim 10^{-5} M_\odot$ and initial magnetic field strength of $\sim 10^{15}$ G. W. C. G. Ho & N. Andersson (2017) further emphasized the need for IE-1613 to have a long-lived ($\gtrsim 10^3$ yr) and spatially extended disk (radius $\gg R_\odot$) with very low accretion rates of the order $\sim 10^{-12} M_\odot \text{ yr}^{-1}$.

Most prior studies rely on supernova fallback to form the initial disk around the NS. Numerical simulations indeed yield sufficient fallback masses from $10^{-4} M_\odot$ to a few $0.1 M_\odot$ (e.g., F. C. Michel 1988; D. N. C. Lin et al. 1991; M. Ugliano et al. 2012; R. Perna et al. 2014; T. Ertl et al. 2020; H.-T. Janka et al. 2022). H.-T. Janka et al. (2022) found net specific angular momenta of the order 10^{16} to $10^{17} \text{ cm}^2 \text{ s}^{-1}$, corresponding to very compact disks with circularization radii of the order 10^6 to 10^8 cm. It should be noted that the net angular momentum in the simulations summarized by H.-T. Janka et al. (2022) comes from the asymmetric supernova mass ejection but not stellar rotation — the latter has been considered by R. Perna et al. (2014). The general conclusion is that the fallback disks are initially very compact with extremely high peak accretion rates of 10^{-6} to $10^{-2} M_\odot \text{ s}^{-1}$ on a timescale of 10 to 10^2 s after the core collapse. It is theoretically unclear if these disks will survive to the very late evolutionary phases of $\gtrsim 10^3$ yr

in order to sufficiently spin down a NS. In fact, R. Perna et al. (2014) argued that these super-Eddington accretion disks may be quickly depleted by very strong radiation driven winds, so they likely do not survive on kyr timescales.

With this said, it is unclear whether the fallback disk model is sufficient in spinning down isolated NSs to the periods of recently observed pulsators. In this paper, we propose an alternative way to create a gas disk around a NS. Our model is based on a binary system where one of the stars explodes in a supernova and the newly created NS can gravitationally capture gas from the shock-impacted, close-by companion star⁶. Our model predicts much more extended disks than the fallback disks considered in previous works, with disk radii evolving from the initial values of the order $10^7 - 10^{11}$ cm to $\gtrsim 1$ AU on kyr timescales.

Our model is schematically described in §2. Then, §3 describes our hydrodynamic simulations of a supernova in a binary system. In §4, we calculate the mass and angular momentum of the gas captured by the NS by post-processing of the simulation, and in §5 we describe the long-term evolution of the accretion disk formed around the NS. Then, in §6, we consider the evolution of the NS spin due to the disk-magnetosphere interactions and present the results on final spin period distribution. §7 discusses these results in the context of ULP observations, and in §8 we summarize our results.

2. OUR MECHANISM

We consider NSs formed from supernovae in binary systems. The vast majority of massive main-sequence stars ($M \gtrsim 10 M_\odot$) relevant for core-collapse supernovae are found in binary, triple, or higher-order systems (D. Raghavan et al. 2010; H. Sana et al. 2012; G. Duchêne & A. Kraus 2013; S. S. R. Offner et al. 2023). The evolution of these massive stars is shaped by various binary mass-transfer effects that could result in stripped-envelope supernovae; there is strong evidence that the progenitor stars for Type Ib/c supernovae lost their Hydrogen envelope via mass transfer with a binary companion (e.g., H. Sana et al. 2012; N. Langer 2012; S. C. Yoon et al. 2012; S. J. Smartt 2015; S. J. Prentice et al. 2018; N. Smith et al. 2011). An important (but the-

⁶ This is not the first time it has been conceptualized that an isolated NS can form an accretion disk from post-supernova-binary-companion interaction. In fact, E. S. Phinney & B. M. S. Hansen (1993) suggested that a NS could be kicked towards its companion, causing it to tidally disrupt and form a disk. Although our model slightly differs, it goes to show that the authors already thought carefully about how a binary-originating NS can become an isolated NS with a disk.

Name	P (s)	b ($^{\circ}$)	DM (pc cm^{-3})	Counterparts	Ref. Paper	Source?
PSR J0250+585	23.5	-0.5	45	None	C. M. Tan et al. (2018)	NS
PSR J0901-4046	76	3.7	52	None	M. Caleb et al. (2022)	NS
AR Scorpii	118	19	(117 pc)	M-Dwarf	T. R. Marsh et al. (2016)	WD
J1912-441	318	-22	(238 pc)	M-Dwarf	I. Pelisoli et al. (2023)	WD
CHIME J0630+25	421	7.1	23	None	F. A. Dong et al. (2024)	?
GLEAM-X J1627	1091	-2.6	57	None	N. Hurley-Walker et al. (2022)	?
GMP-1839	1318	-2.1	274	None	N. Hurley-Walker et al. (2023)	?
ASKAP/DART-J1832	2656	0.1	465–480	X-ray	D. Li et al. (2024)	?
ASKAP-J193	3225	0.7	146	NIR	M. Caleb et al. (2024)	?
GLEAM-X J0704-37	10440	13	37	M-Dwarf	N. Hurley-Walker et al. (2024)	WD
ILT J1101+5521	7350	56	16	M-Dwarf	I. de Ruiter et al. (2024)	WD
IE-1613	24000	-0.4	–	X-Ray	A. De Luca et al. (2006)	NS

Table 1. List of known radio pulsators. From left to right we include their emission period, galactic latitude, dispersion measure, known observed counterparts, the reference paper, and the compact object thought to be responsible for the emission. All are observed in the radio except IE-1613, which is an X-Ray source.

oretically not fully understood) outcome is that about 30% of core-collapse supernovae are from these stripped-envelope stars (e.g., W. Li et al. 2011; M. R. Drout et al. 2011; J. J. Eldridge et al. 2013; J. D. Lyman et al. 2016; F. Taddia et al. 2018; S. E. Woosley et al. 2021). For this reason, we choose to focus on type-Ib/c systems for our paper.

In a binary system, the supernova ejecta will interact with the companion star, which is most likely a main-sequence star. It has been shown through hydrodynamic simulations of core-collapse supernovae that the companion star will be shock heated due to the ejecta’s impact and expand to 5-100 times its original radius (R. Hirai et al. 2014, 2018; M. Ogata et al. 2021; H.-P. Chen et al. 2023). Additionally, assuming that the core-collapse supernova results in a NS, the NS will get a large velocity kick of a few 100 km s^{-1} (G. Hobbs et al. 2005). In most cases, this kick will unbind the NS from its companion, and on its path, it will encounter its companion’s shock inflated envelope. As it passes through the envelope, it will undergo Bondi capture (H. Bondi 1952) (see Figure 1 for the evolution of such a system). The expanded envelope will have a density gradient that may provide enough net angular momentum for Bondi capture compared to the supernova fallback model (see Figure 2).

R. Hirai et al. (2018) studied a system with an initial companion star of mass $10 M_{\odot}$ and radius $5 R_{\odot}$, and separation distances of $20\text{--}60 R_{\odot}$. From largest to shortest separation distances, their companion star inflated to be $30 \sim 200 R_{\odot}$ a short time after explosion. H.-P. Chen et al. (2023) looked at models of separation distance $3\text{--}8 R_{\odot}$ and masses of $3\text{--}8 M_{\odot}$. They also showed that the companion can grow to be about a magnitude larger

than its original size after the shock impact. M. Ogata et al. (2021) found similar results for the same separation distances, with masses of 3 and $15 M_{\odot}$, and ejecta mass of $2 M_{\odot}$. Z.-W. Liu et al. (2015) studied type-Ib/c supernovae with lower ejecta mass of $1.4 M_{\odot}$ impacting on less massive companion stars of 0.9 and $3.5 M_{\odot}$, and they found that the inflation of the shock-impacted companion star strongly depends on the orbital separation.

Since we expect a fraction of the stripped-envelope supernovae to have periods of a few days prior to explosion (P. Podsiadlowski et al. 1992; H. Sana et al. 2012, 2013; A. Gagliano et al. 2022), in this paper we adopt a separation distance of $20 R_{\odot}$ prior to explosion. Furthermore, we will use an ejecta mass of $5 M_{\odot}$, which is consistent with observations of stripped-envelope supernova (C. Barbarino et al. 2021; F. Taddia et al. 2015; M. R. Drout et al. 2011; F. Taddia et al. 2018; J. D. Lyman et al. 2016; S. J. Prentice et al. 2019). We consider a main-sequence companion star of mass $4 M_{\odot}$. We expect our final NS spin period distribution to depend strongly on the orbital separation (and weakly on the companion star mass and ejecta mass), but we leave a detailed exploration of the larger parameter space to a future work. In this paper, we focus on the effects of different NS kick velocities and hence only consider one orbital configuration. Our system has three phases. First, the heating of the companion star by the supernova blast wave is simulated using the hydrodynamic set-up described in §3. Then, the formation of the fallback disk is modeled numerically by post-processing the simulation outputs in §4. Finally, the disk-NS interaction, including the angular momentum transfer between the two, is analytically modeled to late times (up to 10^6 yrs) in §5 and §6.

3. HYDRODYNAMIC SIMULATION

3.1. Setup

We use the hydrodynamic code ATHENA++ (J. M. Stone et al. 2020) to simulate the ejecta-companion interaction, with our code adopted from T. L. S. Wong et al. (2024) and E. B. Bauer et al. (2019). We solve the hydrodynamical equations on a Cartesian grid with a fiducial 512^3 resolution in the co-moving frame of the companion star. A lower 256^3 resolution simulation is performed and the small difference between these two runs justifies the convergence of our results (see Appendix A). We also run the 256^3 resolution simulation for a much longer time to confirm the late-time evolution of the shock-heated star. We adopt an ideal gas equation of state with $\gamma = 5/3$, and utilize the multigrid capabilities of ATHENA++ for self-gravity (K. Tomida & J. M. Stone 2023). Although the supernova ejecta’s pressure is dominated by radiation, here we focus on the response of the companion star. Since most of shock-heated regions are gas pressure-dominated, a choice of $\gamma = 5/3$ provides a reasonable approximation for our problem.

The companion star is taken to be an $n = 3$ polytrope with mass $M_C = 4 M_\odot$ and radius $R_C/R_\odot \approx (M_C/M_\odot)^{0.6}$. The NS progenitor’s mass is the sum of its ejecta and the mass of the NS remnant, $M_{ej} + M_{NS}$. For this paper, we assume a NS mass of $M_{NS} = 1.4 M_\odot$. With an ejecta mass of $M_{ej} = 5 M_\odot$, this gives our pre-explosion star a mass of $6.4 M_\odot$.

The supernova explosion originates from a distance $a_{sep} = 20 R_\odot$ from the companion star’s center, and the ejecta freely expands until hitting the companion star. In ATHENA++, we initialize the outer edge of the ejecta to be $5 R_\odot$ from the center of explosion. The ejecta has a maximum velocity v_{max} of $2 \times 10^4 \text{ km s}^{-1}$ with a total explosion energy $E = 10^{51} \text{ erg}$. The density of the ejecta is taken to be a broken power law as described in R. A. Chevalier & N. Soker (1989) and D. Kasen (2010), with profiles $\rho_i \propto r^{-\delta}$ and $\rho_o \propto r^{-n}$ for the inner and outer regions, respectively. We take δ and n to be 1 and 10, respectively. Assuming an initial orbit in the x-y plane, we give each ejecta fluid element a y-velocity offset to account for the orbital velocities of the two stars prior to explosion. For stars of mass $6.4 M_\odot$ and $4 M_\odot$, we find that the relative velocity between the two stars is 314.9 km s^{-1} .

To model adiabatic cooling, similar to E. B. Bauer et al. (2019), the internal energy of a fluid element at a given time is set to be a fraction of the kinetic energy, dictated by its radius from explosion center r at time t . The kinetic energy density is such that $KE = 1/2 \rho v^2$, where v is the velocity and ρ is the den-

Table 2. Simulation Parameters

Parameter	Label	Value
Grid Size	–	512^3
Domain	–	$x, y, z \in [-20, 20] R_\odot$
Companion Mass	M_C	$4 M_\odot$
Ejecta Mass	M_{ej}	$5 M_\odot$
Ejecta Energy	E	10^{51} ergs
Max Ejecta Velocity	v_{max}	$2 \times 10^4 \text{ km s}^{-1}$
Orbital Velocity	v_{orb}	314.9 km s^{-1}
Separation Distance	a_{sep}	$20 R_\odot$

sity of the fluid element. The pressure at a given radius is $P = (\gamma - 1) \cdot U$, where U is our internal energy density. For adiabatic expansion, the ratio between internal and kinetic energy is $P/(\rho v^2) \propto \rho^{\gamma-1} \propto r^{-3(\gamma-1)} \propto t^{-3(\gamma-1)}$ (for $v = \text{constant}$). Realistically, the SN ejecta is radiation dominated, so we expect $\gamma = 4/3$ and hence $-3(\gamma - 1) = -1$. Using this scaling, we set the internal energy density as $U = KE \cdot r_{equil}/r$, where r_{equil} is the equilibrium radius (at which $KE = U$). Our r_{equil} is $0.08 a_{sep}$, such that as the ejecta reaches the companion its internal energy is $\sim 8\%$ of the kinetic energy.

Lastly, like T. L. S. Wong et al. (2024), we use the passive-scalar capability in ATHENA++ (J. M. Stone et al. 2020), where a passive scalar is a tracer that does not modify fluid properties. Two passive scalars are added, one for the ejecta and one for the companion. This will allow us to distinguish between ejecta and stellar mass captured by the NS later on.

Table 2 summarizes our simulation input parameters.

3.2. Hydrodynamic Results

Figure 1 shows our simulation results at different timesteps. Note that at $t > 40 \text{ hrs}$, we show a lower resolution simulation on a grid of size 256^3 using our previously described parameters. The NS is expected to have a kick on the order of a few hundred km s^{-1} (G. Hobbs et al. 2005), and will no longer interact with the companion envelope by these late times ($> 40 \text{ hrs}$). However, the lower-resolution simulation is ran for a longer duration to confirm the secular expansion of the companion.

As expected, the ejecta interacts with the companion star and the shock-inflation begins within a day of the initial interaction. The companion star eventually relaxes into a spherically symmetric profile with an envelope that expands to several times its original radius by $\sim 1 \text{ week}$. The purpose of this paper is to discuss accretion disk formation around an unbound NS and its subsequent evolution into a ULP, so we will not discuss

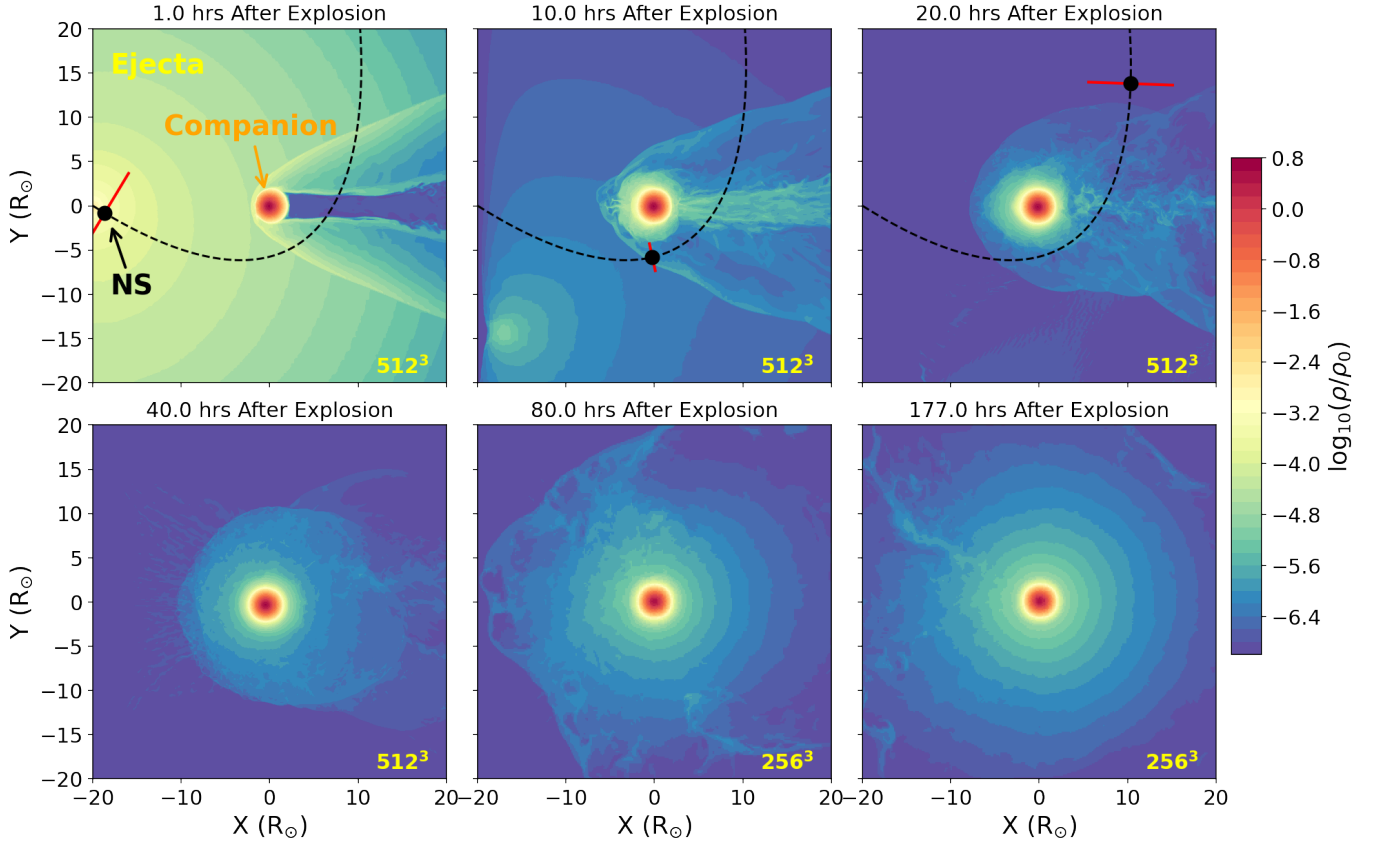


Figure 1. Density slices in the $z = 0$ plane. Overlaid is an example NS trajectory (black dashed line), with a black circle representing the current NS position. In this example, the NS trajectory is inside the x - y plane with a kick velocity 300 km s^{-1} . The red bar represents the critical Bondi radius r_B for gas capture (see Equation 1), dependent on the relative velocity between the NS and the local gas, as well as the local sound speed of the gas. Color indicates gas density in units of $\rho_0 = M_\odot \text{ R}_\odot^{-3}$. The top and bottom left panels are for the fiducial resolution of 512^3 grid (used in this paper). We only ran the 512^3 simulations for ~ 40 hrs, as an unbound NS would not interact with the companion star past this time. The last two panels are for a separate simulation with a lower-resolution 256^3 grid, and is only used to confirm the late-time evolution of the companion.

the companion star long-term evolution on timescales $\gg 1$ day.

Additionally plotted in Figure 1 is an example NS kick trajectory. The NS will pass through and capture gas surrounding the companion star. Note that we do not include the NS gravitational potential in the simulation. Instead, in the following section we post-process the saved data from the simulation to study the gas capture by the NS.

4. MASS CAPTURE

4.1. NS trajectory and Bondi capture

In this section, we consider that a NS is launched from the center of the explosion with original orbital velocity $\vec{v}_{\text{orb}} = v_{\text{orb}} \hat{y}$ plus an additional kick velocity \vec{v}_k . We test 3 different kick amplitudes: 300, 400, and 500 km s^{-1} .

We save 3D snapshots of the simulation, and solve for the NS's kick trajectory within each snapshot. We assume the NS is only influenced by the companion's

gravitational force. The NS's kick trajectory is based on kick amplitude v_k and kick angles θ_k and φ_k as described by Figure 3. Here, $\theta_k = \pi/2 - \theta$ is defined as the latitude angle away from the x - z plane, where θ is the polar angle from the y -axis. The azimuthal angle φ_k is defined as the angle between the projected velocity in the x - z plane and the x -axis. Our final probability density functions are based on the full parameter space of kick angles $\theta_k \in [-\pi/2, \pi/2]$ and $\varphi_k \in [0, 2\pi]$. However, we only consider the kick angles for which the NS becomes unbound from the companion star and ends up isolated (satisfying the constraints on the observed ULPs). We reduce the computation by considering the fact that the entire system is symmetric with respect to the equatorial (x - y) plane; a kick with azimuthal angle φ_k will have the same mass capture as another trajectory with azimuthal angle of $-\varphi_k$. We also assume that no ejecta is captured for kicks away from the companion star ($\pi/2 < \varphi_k < 3\pi/2$), as in those cases, the NS

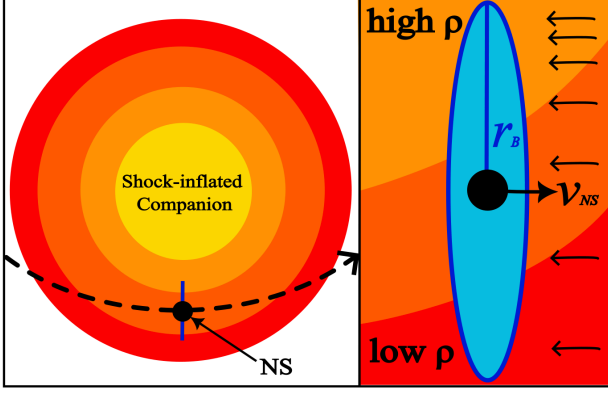


Figure 2. Schematic for gas capture. The panel on the left shows a NS being kicked through its companion's shock inflated envelope. The NS will travel through the expanded envelope of the companion and undergo gas capture described by the Bondi radius r_B (H. Bondi 1952), represented with a blue line. We zoom in on the NS and show the plane for Bondi capture in the right panel. Because the envelope will be more dense towards the companion star's center. In this scenario, there is a density gradient in the captured gas, which provides sufficient angular momentum to circularize into a disk.

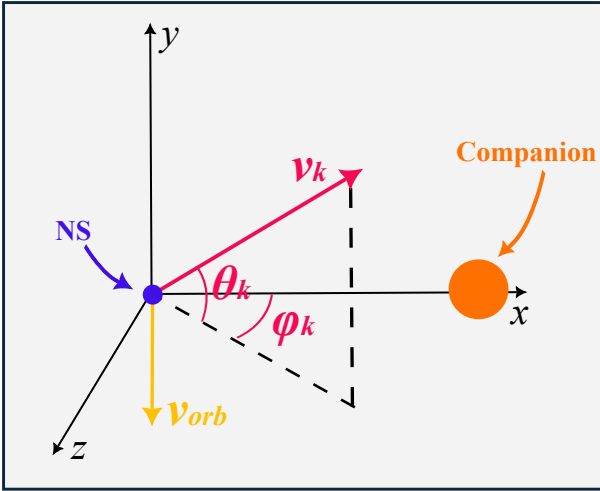


Figure 3. NS Kick Schematic. The companion star is situated along the x-axis. The NS kick velocity is described by magnitude v_k , the latitude angle $\theta_k = \pi/2 - \theta$ away from the x-z plane (where θ is the polar angle from the y-axis), and the azimuthal angle φ_k . In yellow is the orbital velocity vector prior to explosion, $\vec{v}_{orb} = -v_{orb} \hat{y}$. The final initial velocity vector is given by $\vec{v}_{NS} = \vec{v}_{orb} + \vec{v}_k$.

directly moves away from the companion star. Thus, we practically only compute the mass captures for the unbound trajectories for a dense grid of $-\pi/2 < \theta_k < \pi/2$ and $-\pi/2 < \varphi_k < \pi/2$.

As the NS travels, it will gravitationally capture gas that is sufficiently close to its path, as demonstrated in

Figure 2. For mass capture, we adopt a cross section perpendicular to the NS's instantaneous velocity vector with an area of $\sigma = \pi r_B^2$, where r_B is the Bondi radius (H. Bondi & F. Hoyle 1944) approximately given by

$$r_B \approx \frac{2GM_{NS}}{v_{rel}^2 + c_s^2}. \quad (1)$$

Here, G is the gravitational constant, c_s is the sound speed of the fluid element, and $\vec{v}_{rel} = \vec{v}_{NS} - \vec{v}_{fl}$ is the relative velocity between the NS (\vec{v}_{NS}) and the fluid (\vec{v}_{fl}).

Given the NS position and velocity vector, we find which fluid elements undergo Bondi capture at a given time. The rates of mass and angular momentum capture, \dot{M} and \dot{L} , at a given time are given by

$$\dot{M} \approx \int_0^{r_B} dr' \int_0^{2\pi} d\varphi' \rho r' v_{rel}, \quad (2)$$

and

$$\dot{L} \approx \int_0^{r_B} dr' \int_0^{2\pi} d\varphi' \rho r' v_{rel} (\vec{r}' \times \vec{v}_{rel}), \quad (3)$$

where ρ is the density of a given fluid element at position \vec{r}' in the NS's frame. At each time, we consider polar coordinates $\vec{r}' = (r', \phi')$ in the plane perpendicular to the NS's velocity vector (\vec{v}_{NS}). We interpolate the density, pressure, and velocity fields of the fluid elements to obtain their values on a 2D grid of (r', ϕ') in the perpendicular plane, and then sum up the contributions to the mass and angular momentum captures by those fluid elements that satisfy $r' < r_B(r', \varphi')$. Since the fluid velocity v_{fl} and sound speed c_s are typically smaller than the NS velocity, the above approximations are reasonable. Lastly, we exclude any fluid elements that are more gravitationally bound to the companion star than the NS ($M_C/r_C > M_{NS}/r_{NS}$, where r_C is the distance from the companion star center and r_{NS} is the distance from the NS center).

We dump 3D snapshots of the simulation on a time interval of $\delta t = 0.5 \times t_{scale}$, where $t_{scale} = (R_\odot^3/GM_\odot)^{1/2} = 1593 \text{ sec}$ is the time unit used in our simulation. We solve for the position of the NS within each snapshot, and calculate \dot{M} and \dot{L} using Equation 2 and Equation 3. This results in one data point per snapshot. More information on time resolution testing can be found in Appendix A.

An important issue with our approach is that a fraction of the slower moving supernova ejecta is inevitably captured by the NS; this is conceptually similar to the case of fallback accretion. However, due to our simplistic set-up for the spherically symmetric ejecta profile

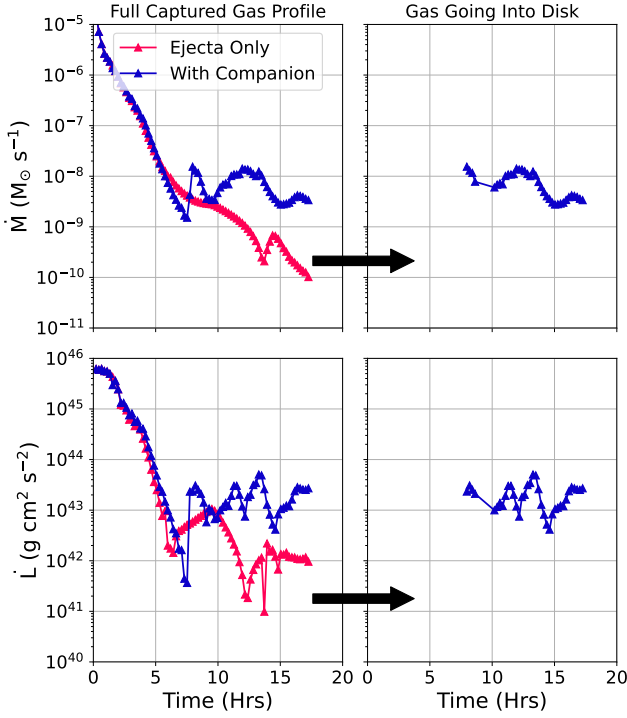


Figure 4. Process of removing fallback accretion. Plotted in blue are the mass- and angular momentum-capture rates using Equation 2 and Equation 3 from our simulations. In red we plot the same for our companion-less simulation (where we allow the ejecta to freely expand). Each data point represents the mass-capture rate per snapshot (every $0.5 \times t_{\text{scale}} = 0.5 \times \sqrt{R_\odot^3/GM_\odot} = 796.5 \text{ sec}$). Data points that differ by a factor of 2 between the two simulations are considered to be “true” mass and angular momentum captured by the NS. The dip in the companion-less simulation results around ~ 13 hours is due to part of the Bondi radius extending outside the simulation domain as the NS passes close to the simulation boundary.

and our ignorance of the radiation pressure (as well as heating sources such as ^{56}Ni), the amount of fallback accretion obtained in our simulation cannot be trusted — a more realistic simulation of the supernova explosion is required to study the realistic fallback accretion. For this reason, we use the following procedure to remove the contribution to the mass and angular momentum capture of the NS from fallback accretion.

To distinguish what is simple free-flowing ejecta, we run a separate simulation similar to the one described in § 3, except we do not include the companion star and instead allow the ejecta to expand freely. We compare the mass-capture rates at each time between the simulations with and without a companion star. We remove the data points where the mass-capture rates between the two simulations are within a factor of two of each other. Since most of the fallback accretion occurs in the first

few hours before the NS reaches close to the companion star, we find that our choice of the threshold for the data removal successfully differentiates between early-time fallback accretion and the late-time mass capture of gas that has been strongly affected by the companion star.

Figure 4 shows an example of mass-capture and angular momentum-capture rates for a given kick velocity as specified by v_k , θ_k , and φ_k . The precise amount removed depends on the NS kick velocity, but we generally find that the removed mass is on the order of $10^{-2} M_\odot$ and that the removed angular momentum is of the order 10^{48} erg s . If this ejecta were to form an accretion disk, it would result in an extremely compact disk with radius $\sim 10^6 \text{ cm}$.

After this filtering process, the total captured mass $M_{d,0}$ is $\sum_n \dot{M}_n \delta t$, where n is the number of data points that survive our fallback-accretion removal procedure, and $\delta t = 0.5 \times t_{\text{scale}}$ is the time resolution of our Bondi-capture calculation. Similarly, $L_{d,0,x} = \sum_n \dot{L}_{x,n} \delta t$, $L_{d,0,y} = \sum_n \dot{L}_{y,n} \delta t$, and $L_{d,0,z} = \sum_n \dot{L}_{z,n} \delta t$.

With our initial disk mass $M_{d,0}$ and angular momentum $L_{d,0} = |\vec{L}_{d,0}|$, the initial radius of the disk $R_{d,0}$ is obtained under the assumption of a circular Keplerian disk

$$L_{d,0} = M_{d,0} \sqrt{GM_{\text{NS}} R_{d,0}}. \quad (4)$$

Therefore, we obtain the total captured mass $M_{d,0}$ and initial circularization radius $R_{d,0}$ for each realization of kick velocity. This allows us to study the subsequent evolution of the accretion disk later in the next section.

Lastly, we use our simulation’s passive scalars to track how much final captured mass comes from the initial ejecta and how much comes from the companion star. Although we evolve our disks using the total captured mass (albeit, with the fallback accretion removed), we are also interested in seeing if a disk and subsequent NS spin-down can be created from the companion’s stellar mass alone. We call these two different types of disk models “total mass disks” and “stellar mass disks.”

4.2. Mass Capture Results

Using our three kick velocities, we calculate the fraction of kick angles that result in unbound and bound NSs. For both the sake of this paper and simplicity, if the NS comes within the initial radius of the companion star, we call this a tidal disruption event (TDE) and remove it from these fractions. We calculate the fraction of unbound NSs to be 0.79, 0.87, and 0.95 for kick amplitudes of 300, 400, and 500 km s^{-1} , respectively. The fraction of bound NSs is 0.19, 0.12, and 0.05 for kick amplitudes of 300, 400, and 500 km s^{-1} , respectively. Meanwhile a fraction of 0.01, 0.01, and 0.001 will

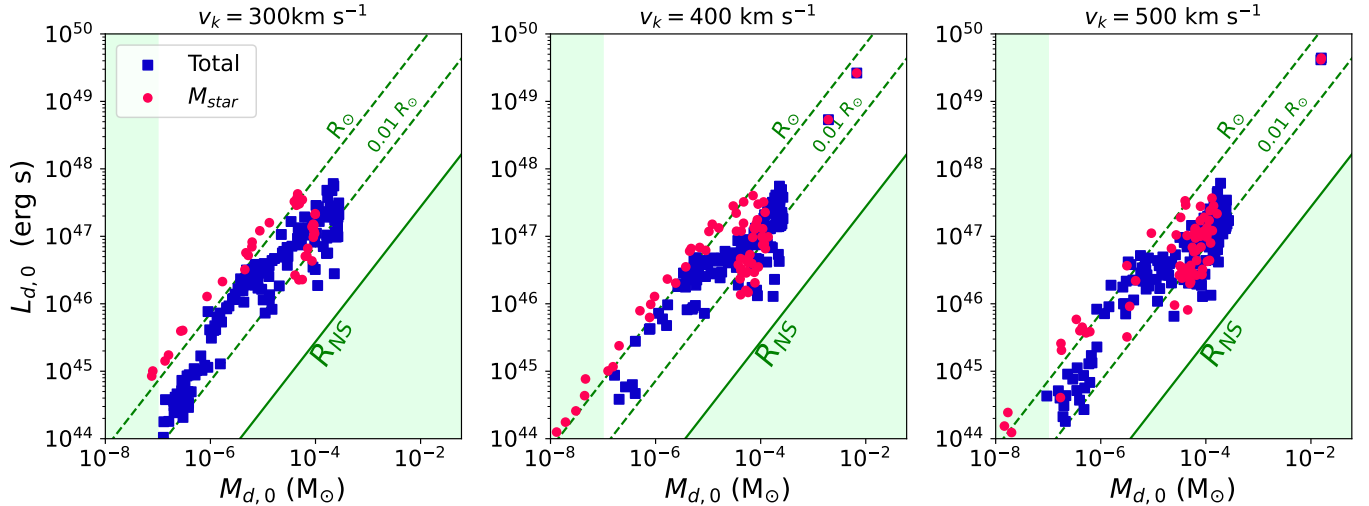


Figure 5. Captured disk masses and angular momenta. Lines of equal radii are plotted using Equation 4. The green shaded regions represent disks that have been disqualified due to our radius cutoff of 10^6 cm and mass cutoff of $10^{-7} M_{\odot}$. Blue squares are of the total disk mass, whereas red circles are disks created considering only companion stellar mass.

result in a TDE for kick amplitudes of 300, 400, and 500 km s^{-1} , respectively.

Not all kick angle realizations will result in a disk that we evolve in § 5. First, in this work, we restrict ourselves to unbound orbits that would lead to an isolated NS, as suggested by ULP observations. Furthermore, to limit uncertainties in the mass capture, we ignore disks that have masses less than $10^{-7} M_{\odot}$ (such low mass disks have little effect on the NS spin anyway). As shown in Figure 5, these limits can disqualify a small fraction of cases. Each data point in Figure 5 represents a different kick angle that are sampled according to a grid of isotropic distribution of kick directions. The disks in our model have masses of $10^{-7} \sim 10^{-2} M_{\odot}$, and angular momentum of $10^{44} \sim 10^{49}$ erg s.

Figure 6 shows the fraction of kick realizations that result in accretion disks, for three different kick velocities. This fraction is taken out of all possible kick angles, where we only count accretion disks that will form around isolated (unbound) NSs. With our limits imposed, we expect to create a disk around an isolated NS 8-10% of the time for our systems. If instead we only consider stellar mass disks, this percentage drops to 2-4%.

Although not always true, much of the contribution of mass and angular momentum of a given disk are from the supernova ejecta fluid elements whose trajectories have been strongly affected by the companion star due to shocks. The NS flies past the companion star on timescales much shorter than the time it takes for the shock-heated outer envelope of the companion star to expand significantly. Thus, the contribution from the stellar mass to the disk is usually small.

In general, lower velocity kicks (300 km s^{-1}) are more likely to form disks, as a higher kick velocity leads to a lower critical radius for Bondi capture (Equation 1). However, we also find that NSs with an initial kick magnitude of 400 km s^{-1} form disks less frequently than 500 km s^{-1} . This is likely because an initial kick velocity of 500 km s^{-1} has a higher probability of resulting in unbound orbits, yet for this higher velocity the companion envelope has not expanded enough for the NS to undergo sufficient gas capture (so the fraction does not exceed the 300 km s^{-1} kick realizations).

5. DISK EVOLUTION

After acquiring our disk masses and circularization radii, we analytically solve for the evolution of each disk, which viscously spread and accrete onto the NS. Our goal is to solve for the time evolution of the disk mass $M_d(t)$, disk radius $R_d(t)$, and mass accretion rate $\dot{M}_d(t)$. We adopt the simplest one-zone model (R.-F. Shen & C. D. Matzner 2014) which captures most of the physics governing the long-term evolution of the disk. The interactions between the disk and the NS magnetosphere are considered in a postprocessing manner, as we expect the effects of accretion feedback on the evolution of the outer disk to be negligible. We assume that the disk rotates near the Keplerian speed and is in hydrostatic equilibrium in the vertical direction.

We find that each of our disks have different mixes of contributions from the ejecta and companion stellar mass, resulting in varying types of chemical compositions. Throughout this section, we assume a solar abundance; however, we note that the disk composition is not

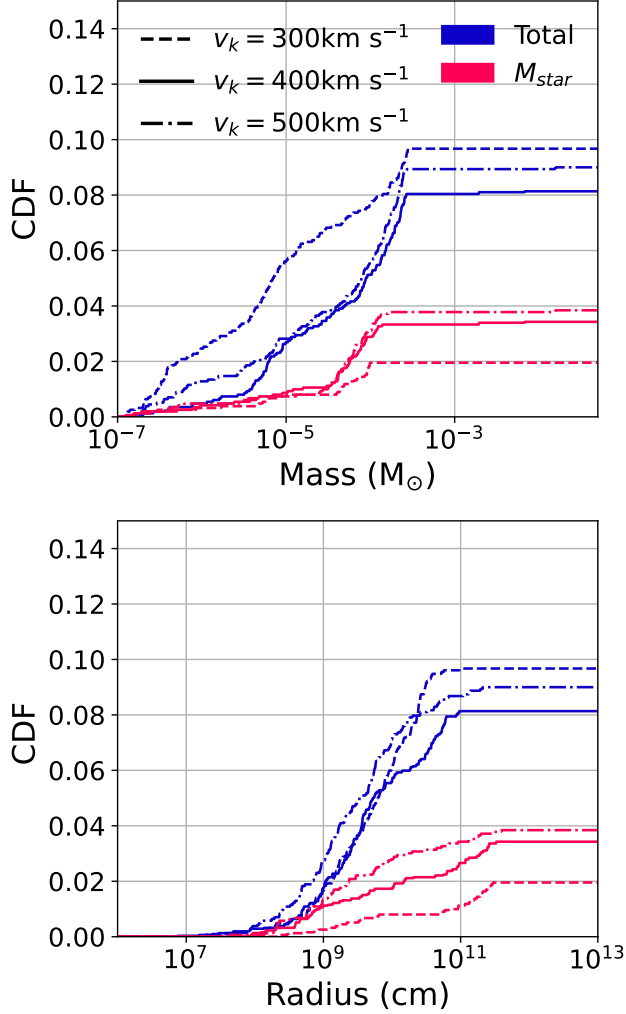


Figure 6. Fraction of disks formed for three kick velocities: 300, 400, and 500 km s⁻¹. Out of all possible kicks ($\theta_k = [-\pi/2, \pi/2]$, $\varphi_k = [0, 2\pi]$), we calculate the fraction of disks formed in unbound orbits that have mass greater than $10^{-7} M_\odot$, and circularization radius greater than 10^6 cm. Blue represents the disks we calculate in §4, whereas red represents the disks created considering only companion stellar mass.

exactly solar because of the captured Hydrogen-deficient ejecta.

At any given time t , the mid-plane sound speed c_s , scale-height H , Keplerian angular velocity Ω_k , and the surface density Σ of the disk are given by

$$c_s^2 = \frac{P}{\rho}, \quad H = \frac{c_s}{\Omega_k}, \quad (5)$$

$$\Omega_k = \left(\frac{GM_{NS}}{R_d^3} \right)^{1/2}, \quad \frac{M_d}{\pi R_d^2} = \Sigma = 2\rho H, \quad (6)$$

with pressure P and density ρ . The shear viscosity is given by the N. I. Shakura & R. A. Sunyaev (1973) α -

prescription:

$$\nu_{vis} = \alpha c_s H.$$

Motivated by the observations of dwarf novae, previous works have considered a variable α model (J.-M. Hameury et al. 1998; S. Ichikawa & Y. Osaki 1992; E. T. Vishniac & J. C. Wheeler 1996). We follow the method in J.-M. Hameury et al. (1998) by adopting

$$\log \alpha = \log \alpha_{\text{cold}} + (\log \alpha_{\text{hot}} - \log \alpha_{\text{cold}}) \times \left[1 + \frac{2.5 \times 10^4 \text{ K}}{T} \right]^{-1}, \quad (7)$$

where $\alpha_{\text{hot}} = 0.1$ represents a disk in the hot regime, and $\alpha_{\text{cold}} = 0.02$ represents the cold regime. T is the mid-plane temperature of the outer disk near radius R_d . We further note that α changes with gas composition in the disk (M. S. B. Coleman et al. 2018), however, we show in Appendix C that our final results do not depend strongly on the α prescription we use.

The pressure P comes from radiation pressure and gas pressure such that $P = P_{\text{gas}} + P_{\text{rad}}$. With Boltzmann constant k_B , radiation constant a , mean molecular weight μ (fixed to be 0.6), and proton mass m_p , the pressure in the disk mid-plane is:

$$P = \frac{\rho k_B T}{\mu m_p} + \frac{a T^4}{3}. \quad (8)$$

We solve for the mid-plane temperature T from the equation of thermal equilibrium, with viscous (q_{vis}^+) and irradiative (q_{irr}^+) heating balancing radiative (q_{rad}^-) and advective (q_{adv}^-) cooling, i.e.,

$$q_{\text{vis}}^+ + q_{\text{irr}}^+ = q_{\text{adv}}^- + q_{\text{rad}}^-. \quad (9)$$

We follow R.-F. Shen & C. D. Matzner (2014) for the expressions for q_{vis}^+ , q_{rad}^- , and q_{adv}^- , and add irradiation effects from NS X-ray emission (e.g., Ü. Ertan et al. 2009; M. A. Alpar et al. 2013). We assume a constant X-ray luminosity of $L_x = 10^{35}$ erg s⁻¹, which is reasonable among known magnetars⁷. The irradiative heating rate is taken to be

$$q_{\text{irr}}^+ = \frac{1}{5} \frac{L_x}{4\pi R_d^2} \frac{H}{R_d}, \quad (10)$$

which is derived from the disk's flared geometry in Appendix B.

Putting everything together, the equation of thermal equilibrium is given by

$$\frac{9}{4} \nu_{vis} \Sigma \Omega_k^2 + \frac{1}{5} \frac{L_x}{4\pi R_d^2} \frac{H}{R_d} = \frac{M_d/t_{\text{vis}}}{2\pi R_d^2} \frac{P}{\rho} + \frac{4acT^4}{3\kappa\Sigma}, \quad (11)$$

⁷ See the magnetar catalog: <http://www.physics.mcgill.ca/~pulsar/magnetar/main.html>

where c is the speed of light and κ is the temperature-dependent Rosseland-mean opacity. The opacity κ is taken from the OPAL project (C. A. Iglesias & F. J. Rogers 1996) for temperatures $T \gtrsim 10^4$ K and J. W. Ferguson et al. (2005) for $T \lesssim 10^4$ K (including the effects of molecules and dust grains). We assume a solar composition.

We solve the above equation for the mid-plane temperature T , which then tells us the vertical scale-height H and hence the viscous timescale,

$$t_{vis} = \frac{\alpha}{\Omega} \left(\frac{H}{R_d} \right)^{-2}. \quad (12)$$

The time evolution of the system is governed by the viscous timescale.

Finally, the equations of mass and angular momentum conservations are given by

$$\dot{M}_d = -\frac{M_d}{t_{vis}} + \dot{M}_{cap}(t), \quad (13)$$

and

$$\dot{L}_d = \dot{L}_{cap}(t), \quad (14)$$

where the mass capture rate during disk formation is given by $\dot{M}_{cap}(t) = M_{d,0}/t_0$ for $t < t_0$ and $\dot{M}_{cap}(t) = 0$ for $t > t_0$. The angular momentum capture rate is given by $L_{cap}(t) = \dot{M}_{cap}(t)\sqrt{GM_{NS}R_{d,0}}$. For simplicity, we fix $t_0 = 20$ hrs to be the duration for the initial mass capture phase for all kick angles. We expect our results to not depend strongly on our choice of t_0 because the spin evolution of the NS only depends on the late-time ($t \gg 1$ yr) evolution of the disk. The angular momentum conservation equation, combined with the assumption of Keplerian rotation, gives the time evolution of the outer disk radius

$$\frac{\dot{R}_d}{2R_d} = \frac{1}{t_{vis}} + \frac{\dot{M}_{cap}}{M_d} \left(\sqrt{R_{d,0}/R_d} - 1 \right). \quad (15)$$

We track the evolution of each disk realization with the captured masses and circularization radii from Figure 5. The evolution of one such disk is shown in upper and middle panels of Figure 7, where we see that the disk undergoes two important state transitions. First, the disk goes from a radiation pressure-dominated (geometrically thick) regime to a gas pressure-dominated (geometrically thin) regime on a timescale of $t_0 = 20$ hrs as mass is no longer being added to the system. Second, once the gas in the mid-plane of the disk cools below $\sim 10^4$ K, the opacity rapidly drops due to hydrogen recombination (see H.-R. Yang et al. 2024, for a similar evolution) and the disk further collapses into an even thinner one. We note that if we instead assumed a

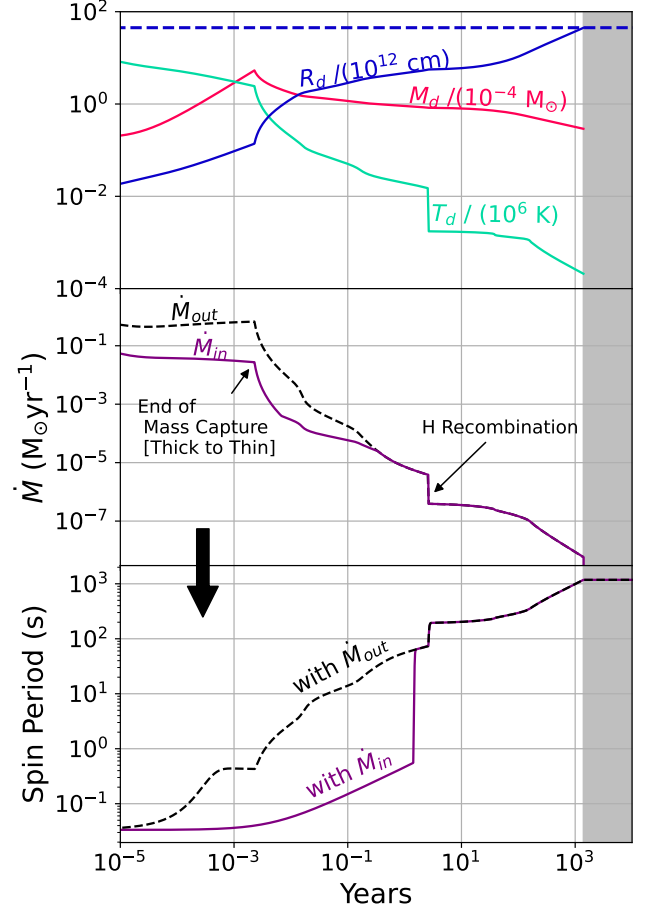


Figure 7. Temperature, mass, radius, and accretion rate evolution of one of our disks. The dashed horizontal line in the top panel represents the irradiation radius, in which we stop disk evolution and consider the disk to be evaporated. We include the accretion rate in the outer disk \dot{M}_{out} and that in the inner disk \dot{M}_{in} near the Alfvén radius (taking into account mass loss due to super-Eddington wind, see §6). The accretion rate suddenly drops in two locations: where the disk goes from thick to thin regime as mass is no longer being added to the disk, and when the opacity becomes dominated by hydrogen recombination. We further plot the spin period evolution, using our \dot{M}_{in} values and methods described in §6.

Hydrogen-deficient gas composition, Helium recombination would set in at a higher temperature, and the disk would collapse at an earlier time. This may change the onset of the “propeller phase” (when the NS rapidly spins down, see §6), but the NS long-term evolution would follow the equilibrium spin period described in §6, and we do not expect our final spin results to be substantially affected.

When the outer disk viscously evolves to even larger radii (a few to 10 AU), it is expected that the disk will experience photo-evaporation due to the NS’s X-

ray emission (J. E. Owen et al. 2012). The details of the photo-evaporation process are complex as the mass-loss rate due to evaporation depends on the surface temperature T_s of the disk under X-ray heating (M. C. Begelman et al. 1983). When the sound speed of the photo-heated surface layer reaches a significant fraction of the local escape speed, we expect the gas to escape the system as a result of vertical expansion and subsequent heating due to X-ray heating. Thus, the disk evaporates when its outer radius reaches a fraction of the following characteristic radius

$$r_{\text{evap}} = \frac{2\mu m_p GM_{\text{NS}}}{k_B T_s} = 6.0 \text{ AU} \left(\frac{T_s}{3 \times 10^4 \text{ K}} \right)^{-1}, \quad (16)$$

where T_s is the temperature of the evaporating surface layer that is heated due to direct X-ray irradiation. In our model, we account for the effect of photo-evaporation by imposing a maximum disk radius $R_{\text{d,max}} = 3 \text{ AU}$. This means that we truncate the disk evolution once $R_d > R_{\text{d,max}}$ and we no longer consider its effects on the NS's spin. By the time the outer disk reaches such a large radius, the mid-plane temperature has cooled down to a typical temperature of $\lesssim 100 \text{ K}$ and is believed to become passive anyway (e.g., S.-i. Inutsuka & T. Sano 2005). We find that the disk truncation due to photo-evaporation generally occurs much later than the propeller phase during which the NS rapidly spins down (see §6), so our results of ULP formation are robust against the details of photo-evaporation.

6. NEUTRON STAR SPIN

6.1. Spin Evolution

Once the disk evolution is obtained, we then consider the interactions between the disk and the NS magnetosphere. We first define the light cylinder radius r_{lc} , the corotational radius r_{co} , and the Alfvén radius r_A (P. Ghosh & F. K. Lamb 1978) as

$$r_{lc} = c/\Omega \quad (17)$$

$$r_{co} = (GM/\Omega^2)^{1/3} \quad (18)$$

$$r_A = \left(\frac{3B^2 R^6}{2\dot{M}_{in} \sqrt{GM}} \right)^{2/7}, \quad (19)$$

where Ω is the spin angular frequency of the NS, and \dot{M}_{in} is the accretion rate of the inner edge of the disk at the Alfvén radius.

At early times when the accretion rates are super-Eddington, mass removal by disk winds causes \dot{M}_{in} to be different from the accretion rate of the outer disk, which is given by

$$\dot{M}_{out} = \dot{M}_d / t_{vis}. \quad (20)$$

The characteristic radius for winds driven by super-Eddington radiation is the spherization radius (N. I. Shakura & R. A. Sunyaev 1973)

$$r_{sph} = GM_{NS} \dot{M}_{out} / L_{Edd}, \quad (21)$$

where $L_{Edd} = M_{NS} G \pi m_p c / \sigma_T$ is the Eddington luminosity of the system. The disk is geometrically thick at radii $r < r_{sph}$ and a strong wind is expected, causing the true accretion rate to drop towards smaller radii as a power-law $\dot{M} \propto r^p$ (R. D. Blandford & M. C. Begelman 1999), where p is typically 0.3 - 1 according to numerical simulations (F. Yuan et al. 2012). In this paper, we take $p = 0.5$ as motivated by more recent simulations (M. Guo et al. 2024; H. Cho et al. 2024; D. Toyouchi et al. 2024).

If $r_A > r_{sph}$, the effects of disk wind are negligible so we take $\dot{M}_{in} = \dot{M}_{out}$ for a steady-state disk. However, if $r_A < r_{sph}$, the mass loss due to wind reduces the accretion rate near the Alfvén radius such that

$$\dot{M}_{in} = \dot{M}_{out} \left(\frac{r_A}{\min(r_{sph}, R_d)} \right)^p. \quad (22)$$

Using the accretion rate in the inner disk in Equation 19, we obtain the modified Alfvén radius

$$r_A = \left(\frac{3B^2 R^6}{2\dot{M}_{out} \sqrt{GM_{NS}}} \right)^{\frac{1}{p+7/2}} [\min(r_{sph}, R_d)]^{\frac{p}{p+7/2}}. \quad (23)$$

The torques on the NS depend on the order of these three radii r_{lc} , r_{co} , and r_A .

If r_A is greater than r_{lc} , then the NS will not interact with the disk and will act as an isolated pulsar. The disk begins to interact with the NS's magnetic field if $r_A \leq r_{lc}$, which causes a torque on the NS from the disk $\dot{\Omega}_{disk}$ (K. Davidson & J. P. Ostriker 1973; P. Ghosh & F. K. Lamb 1978). If the inner disk is moving faster than the rotational velocity of the NS ($r_{co} > r_A$), then the NS will experience a positive, spin-up torque. On the other hand, if $r_{co} < r_A$, then the NS will experience a negative torque that acts to slow the NS down; this is referred to as the “propeller phase.”

Whether or not the disk interacts with the magnetic field, there will also be a spin-down torque on the NS due to magnetic dipole emission alone, denoted as $\dot{\Omega}_{mag}$. The magnitude of this torque depends on whether r_A is greater than or less than r_{lc} . When the disk crosses into the magnetosphere, some field lines become open (K. Parfrey et al. 2016; B. D. Metzger et al. 2018), which exert an additional torque.

At a given time, the time evolution of the NS's spin angular frequency, $\dot{\Omega} = \dot{\Omega}_{disk} + \dot{\Omega}_{mag}$, is summarized by the following equations:

$$r_A > r_{lc} : \dot{\Omega}_{disk} = 0, \quad \dot{\Omega}_{mag} = -\frac{B^2 R^6 \Omega^3}{I c^3}, \quad (24)$$

$$r_A \leq r_{lc} : \dot{\Omega}_{disk} = \frac{\dot{M}_{in} \sqrt{GM_{NS} r_A}}{I} \left(1 - (r_A/r_{co})^{3/2} \right),$$

$$\dot{\Omega}_{mag} = -\frac{B^2 R^6 \Omega^3}{I c^3} (r_{lc}/r_A)^2, \quad (25)$$

where whether the disk is spun up or down is encrypted in the $1 - (r_A/r_{co})^{3/2}$ term (see also K. Y. Ekşi et al. 2005; A. L. Piro & C. D. Ott 2011).

When the system is in the propeller regime ($r_{lc} > r_A > r_{co}$), there are two spin-down torques, one from the disk ($\dot{\Omega}_{disk}$) and the other one from the magnetic fields ($\dot{\Omega}_{mag}$). The ratio between the two spin-down torques is given by

$$\frac{|\dot{\Omega}_{disk}|}{\dot{\Omega}_{mag}} = \frac{3}{2} \left(\frac{r_A}{r_g} \right)^{1/2},$$

where $r_g = GM_{NS}/c^2$ is the gravitational radius of the NS. In our model, since $r_A \gg r_g$, the disk torque always dominates over the magnetic torque during the propeller phase. When the disk interacts with the magnetosphere for a sufficiently long time, the NS spin comes to an equilibrium rate Ω_{eq} given by $r_{co} = r_A$ (ignoring $\dot{\Omega}_{mag}$ in the propeller phase):

$$\Omega_{eq} = (GM_{NS})^{5/7} \left(\frac{2\dot{M}_{in}}{3B^2 R^6} \right)^{3/7}$$

$$= 4.8 \times 10^{-2} \text{ rad s}^{-1} \left(\frac{\dot{M}_{in}}{10^{-8} M_{\odot} \text{ yr}^{-1}} \right)^{3/7} B_{14}^{-6/7}. \quad (26)$$

The scalings of $\Omega_{eq} \propto \dot{M}_{in}^{3/7} B^{-6/7}$ means that, when the system reaches the equilibrium state, the slowest spins are achieved at low accretion rates and strong B-fields. In fact, it is believed that NSs in high-mass X-ray binaries reach very long spin periods (up to many hours) as a result of the propeller effect due to a negative $\dot{\Omega}_{disk}$ (e.g., L. Stella et al. 1986). Turning the argument in Equation 26 around, we can solve for the critical accretion rate corresponding to the equilibrium state at a given spin period

$$\dot{M}_{cr} = \frac{3B^2 R^6 \Omega^{7/3}}{2(GM)^{5/3}}$$

$$= 5.7 \times 10^{-11} M_{\odot} \text{ yr}^{-1} B_{14}^2 \left(\frac{P}{10^3 \text{ s}} \right)^{-7/3}, \quad (27)$$

where $B_{14} = B/10^{14}$ G. We note that other works have different torque models for Ω_{disk} . In the literature, the term $1 - (r_A/r_{co})^{3/2}$ often becomes $1 - \omega^n$, where $\omega = (r_A/r_{co})^{3/2}$ is referred to as the “fastness” parameter. We take n to be 1 in our calculations, however,

works such as A. A. Gençali et al. (2022), A. A. Gençali et al. (2023) took $n = 2$. Our final period distribution does not depend on the choice of n , which only affects how rapidly the spin rate evolves towards Ω_{eq} (Equation 26) when the system enters the propeller phase. This is because we always find that the NS quickly reach Ω_{eq} soon after the propeller phase (on a timescale much shorter than the disk evolution timescale, see Figure 8).

Lastly, our model includes the effect of magnetic field strength decay over time. There are multiple causes for field decay, including Ohmic decay, the Hall effect, and ambipolar diffusion (e.g., P. Goldreich & A. Reisenegger 1992; J. A. Pons & U. Geppert 2007). As we consider NSs with $B \geq 10^{13}$ G, it is expected that the magnetic field decay will be dominated by the ambipolar diffusion of the solenoidal component on a timescale of (P. Goldreich & A. Reisenegger 1992)

$$\tau_{ambip} = 3 \times 10^5 \text{ yr}^{-1} \frac{L_5^2 T_{c,8}^2}{B_{14}^2}, \quad (28)$$

where $L_5 = L/10^5$ km is the length scale for magnetic field variations (we take $L_5 = 1$), $B_{14} = B/10^{14}$ G is our magnetic field strength at a given time, and $T_{c,8} = T_c/10^8$ K is the core temperature at a given time. Thus, $B(t)$ will depend on core temperature $T_c(t)$, according to $dB/dt \sim -B/\tau_{ambip}$. The core temperature evolution is controlled by magnetic field decay heating and cooling due to neutrino and surface photon emission. We follow W. Lu et al. (2022) by taking the magnetic field heating rate $L_B \simeq V_{core} B^2 / (8\pi\tau_{ambip})$ (where $V_{core} \simeq 4 \times 10^{18} \text{ cm}^3$ is the volume of the outer core), photon cooling rate $L_{\gamma} \sim 9 \times 10^{33} T_{c,8.5}^{2.2} \text{ erg s}^{-1}$ (E. H. Gudmundsson et al. 1982; D. Page et al. 2004), and the neutrino cooling rate $L_{\nu} \sim 5 \times 10^{35} T_{c,8.5}^8 \text{ erg s}^{-1}$ (S. L. Shapiro & S. A. Teukolsky 1983).

At early times and temperatures $T_c \gg 10^8$ K, the cooling will be dominated by neutrino emission. In this regime, if $L_{\nu} > L_B$, the temperature goes as $T_c \simeq 10^{8.5} (t/\text{kyr})^{-1/6}$ K. If magnetic decay heating dominates ($L_{\nu} < L_B$), then the temperature will plateau at $T_c \simeq 2.8 \times 10^8 B_{15}^{0.4} L_5^{-0.2}$ K. At late time $t \geq t_{tr} \sim 6 \times 10^4$ yrs (found when $L_{\nu} = L_{\gamma}$), if $L_{\gamma} > L_B$, then the temperature will go as $T_c \simeq T_{tr} (t/t_{tr})^{-5}$ K, where $T_{tr} \simeq 1.5 \times 10^8$ K is the temperature at $t = t_{tr}$. If heating dominates ($L_{\gamma} < L_B$), then the temperature will plateau at $T_c \simeq 0.7 \times 10^8 B_{14}^{0.95} L_5^{-0.48}$ K.

We numerically solve for $T_c(t)$ and $B(t)$. Using this and the inner disk accretion rate $\dot{M}_{in}(t)$ from §5, we calculate the torques on the NS and hence the spin period evolution for a given initial period P_0 . We evolve the system until 1 Myr, beyond which the disk would either evaporate or become passive. We also note that

our results do not depend strongly on the magnetic field decay prescription (see Appendix D). This is because most ULPs are produced within 10^3 yr after the NS formation (see Figure 8), which is typically shorter than the magnetic field decay timescale.

6.2. Spin Period Results

We consider two initial spin periods of $P_0 = 0.033$ s and $P_0 = 0.1$ s. The initial spin period sets the light-cylinder radius r_{lc} , which in turn governs if the disk interacts with the NS. However, once the NS enters the propeller phase, the system will evolve to reach the equilibrium spin rate Ω_{eq} (independent of P_0 , see Equation 26), so our results are largely insensitive to the initial spin periods if the magnetic field is sufficiently large.

Figure 8 shows the period evolution of all disks for NS kick velocity $v_k = 400$ km s $^{-1}$, initial spin period $P_0 = 0.033$ s, and initial B-field strengths 10^{13} , 10^{14} , and 10^{15} G. We find a bi-modal distribution of spin periods. The short-period mode is for NSs that never interact with the accretion disk and evolve as regular isolated pulsars. The second mode is for NSs that undergo the propeller phase within the first \sim kyr of their lifetimes, resulting in a long spin period by 1 Myr. Our models show that the NS is in the propeller phase for a short amount of time, and rapidly spins down as it reaches the equilibrium period described by Equation 26. We zoom in on one random disk in Figure 8 to show this short-term evolution. For this one example, the NS rapidly spins down around $t \simeq 200$ yr and reaches a final period of $P \simeq 10^4$ s at $t \gtrsim 10$ kyr.

We study the spin-period evolution for the three initial kick velocities above, and tested seven different initial magnetic field strengths, ranging from 10^{13} to 10^{16} G in steps of 0.5 in log space. Figure 9 and Figure 10 show the cumulative distribution of spin periods by the end of our disk evolution at 1 Myr for the initial spin periods of 0.33 s and 0.10 s, respectively. We see the same bimodal distribution that is highlighted in Figure 8: some pulsars never interact with an accretion disk and remain in the short-period mode, whereas others undergo the propeller phase during their evolution and end up in the long-period mode.

For stronger NS magnetic fields, we observe more ultra-long period pulsars. This is because a stronger magnetic field would extend the influence of the magnetosphere and increase the torque the disk provides on the NS. We do not observe any ultra-long period pulsars (defined as $P \geq 10^3$ s for our purposes) for NSs with initial B-field strengths $\leq 10^{14}$ G when $P_0 = 0.033$ s, though a very small fraction do undergo the propeller phase. However, when we increase the initial spin pe-

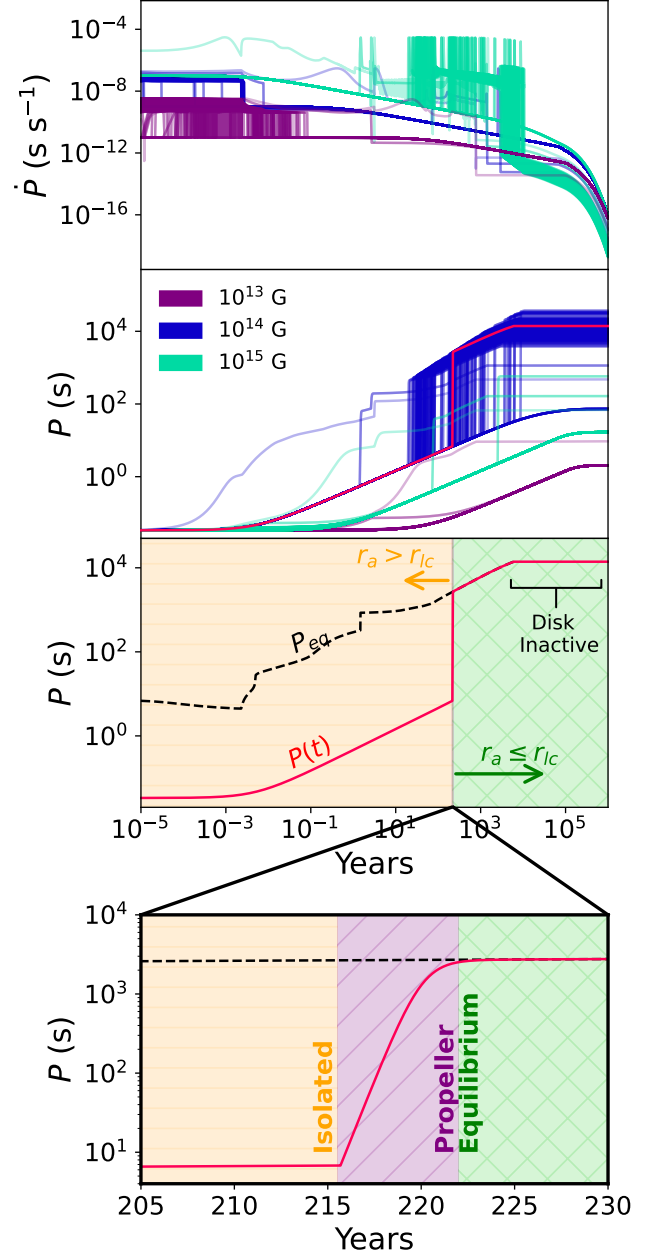


Figure 8. Period evolution for all disks formed from an initial kick velocity of $v_k = 400$ km s $^{-1}$, initial spin period $P_0 = 0.033$ s, and initial B-field strength of 10^{13} G, 10^{14} G, and 10^{15} G. Disks presented are formed from total mass capture. For disks undergoing the propeller phase, it appears they undergo a sudden jump in period. However, we zoom in on one of the systems (indicated in red), plotted with the equilibrium period calculated from Equation 26. The sudden jump is physical and is from the nature of log-space. In reality, the NS reaches the equilibrium spin period over several years. Meanwhile, the early-time fluctuations in \dot{P} for $B_0 = 10^{13}$ G is understood to be from r_A being within r_{lc} , and then \dot{P} suddenly drops as the disk viscously spreads and $r_A > r_{lc}$.

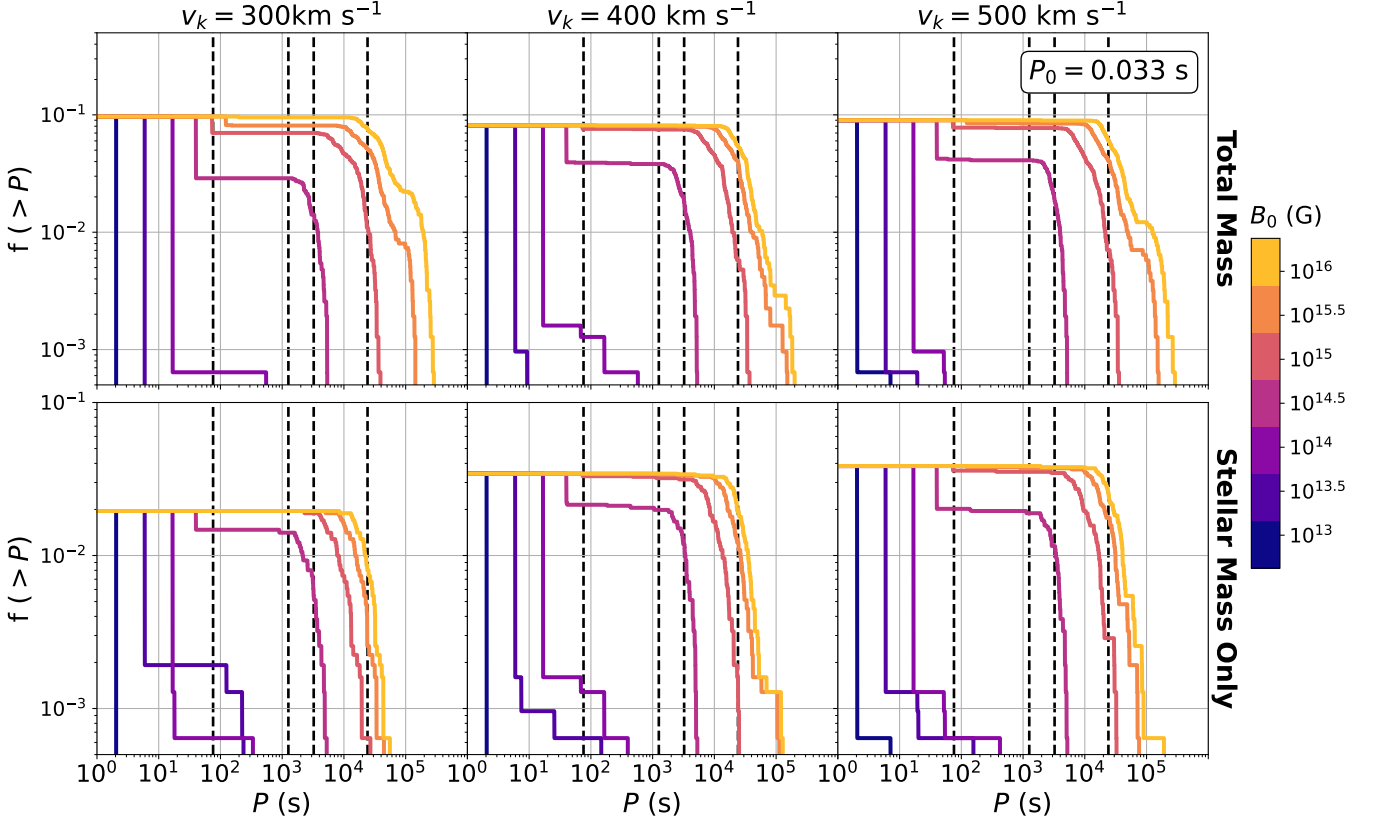


Figure 9. Cumulative Distribution Plot of Spin Periods for $P_0 = 0.033$ s. Fractions are taken out of all possible kick angles. Columns are of different initial kick velocities, with the top row being for disks considering the total mass captured, and the bottom row being disks if we only considered stellar matter. Color indicates initial B-field strength. Dashed lines represent observed radio transients, PSR J0901-4046 at 76 s, GMP-1839 at 21 min, ASKAP-J1935 at 54 min, and IE-1613 at 6.7 hrs.

riod from $P_0 = 0.033$ s to $P_0 = 0.1$ s, the fraction of low magnetic field NSs that enter the propeller phase increases. It is possible to achieve pulsars with periods on the order of $\sim 10^2$ s with lower magnetic field strengths $\leq 10^{13.5}$ G and periods on the order $\sim 10^3$ s with magnetic field strengths $\sim 10^{14}$ G if we start with a higher initial period. For magnetic fields $\gtrsim 10^{14.5}$ G, our results are practically identical between the two initial spin periods.

In Table 3, we report on the fractional occurrence rate of final spin periods for each magnetic field strength. We also include the largest spin period achieved in our simulations. Based on these values, we find that the initial period can affect the largest spin period achieved for lower initial magnetic fields ($B_0 = 10^{13}$ G, $10^{13.5}$ G, and 10^{14} G). In fact, the spin periods for given cumulative occurrence fractions $f(>P)$ for $P_0 = 0.1$ s are about 10 times longer than those for $P_0 = 0.033$ s. However, for $B_0 \gtrsim 10^{14.5}$ G, the two initial periods do not lead to major differences in the final distribution for long-period pulsars (within runoff margins).

The period distribution of pulsars depends strongly on the initial magnetic field strength B_0 . For example,

using $P_0 = 0.033$ s, we only observe periods up to ~ 500 s (although rarely produced) for $B_0 = 10^{14}$ G. For a stronger initial field of $B_0 = 10^{14.5}$ G, the maximum NS period increase to roughly 5×10^3 s. Longer periods ($P \gtrsim 10^4$ s) are produced for $B_0 \gtrsim 10^{15}$ G.

Figure 11 shows the final period's dependence on the disk properties, including the total captured mass, initial circularization radius, and disk accretion rate at $t = t_0 = 20$ hr (chosen to be the end of disk assembly). We find that, for a given initial B-field strength, the final spin period is longer for *lower* captured mass. This counter-intuitive result can be understood as follows. A higher captured mass makes it more likely for the system to enter the propeller phase and hence produce an ultra-long period pulsar. However, once the propeller phase is achieved, the NS quickly reaches the equilibrium spin period $P_{eq} = 2\pi/\Omega_{eq} \propto \dot{M}^{-3/7} B^{6/7}$ (Equation 26), so the final period is longer for lower accretion rates. Lower accretion rates are achieved with smaller mass disks.

We note that our spin rates are calculated at 1 Myr and that not all ULPs are assumed to be at this age. However, we find that the accretion disks slow down the NSs within the first 10 kyr (see Figure 8). For ages

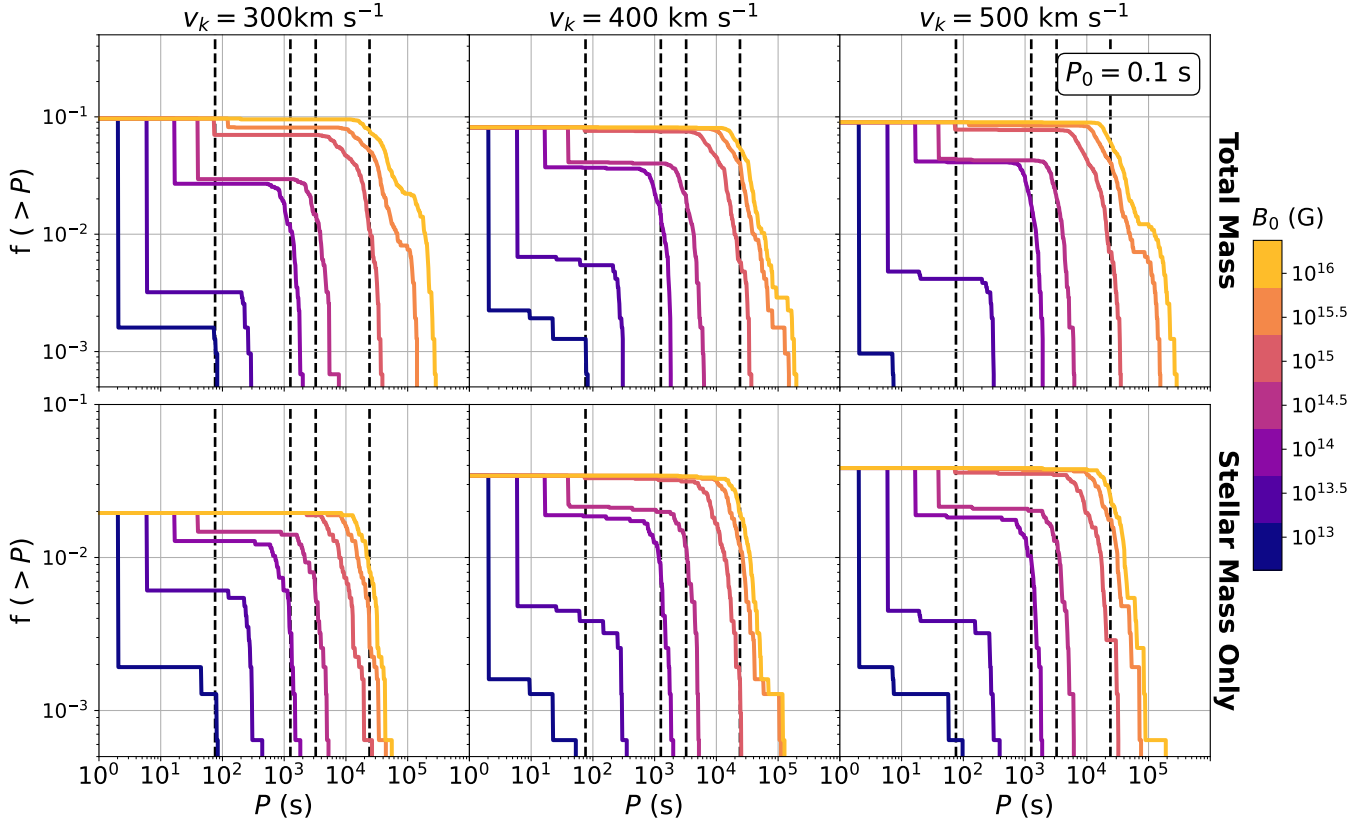


Figure 10. Same as Figure 9, but for $P_0 = 0.1$ s.

	$f(>P)$	13	13.5	14	14.5	15	15.5	16
$P_0 = 0.033$ s	5×10^{-2}	2.0	5.9	1.7×10^1	4.0×10^1	9.2×10^3	2.7×10^4	4.4×10^4
	10^{-2}	2.0	5.9	1.7×10^1	4.1×10^3	2.5×10^4	6.8×10^4	1.9×10^5
	5×10^{-3}	2.0	5.9	1.7×10^1	4.6×10^3	3.1×10^4	1.2×10^5	2.2×10^5
	10^{-3}	2.0	9.4	1.7×10^2	5.3×10^3	3.7×10^4	1.5×10^5	2.7×10^5
	max P	9.4	2.5×10^1	5.8×10^2	5.4×10^3	3.9×10^4	1.6×10^5	2.9×10^5
$P_0 = 0.1$ s	5×10^{-2}	2.0	6.0	1.7×10^1	4.0×10^1	9.2×10^3	2.6×10^3	4.4×10^3
	10^{-2}	2.0	6.0	1.5×10^3	4.4×10^3	2.5×10^4	6.8×10^4	1.9×10^5
	5×10^{-3}	2.0	2.2×10^2	1.7×10^3	4.9×10^3	3.1×10^4	1.2×10^5	2.2×10^5
	10^{-3}	8.0×10^1	3.1×10^2	1.9×10^3	6.2×10^3	3.6×10^4	1.5×10^5	2.7×10^5
	max P	8.3×10^1	3.1×10^2	2.0×10^3	8.7×10^3	3.9×10^4	1.6×10^5	2.9×10^5

Table 3. Final spin period results from Figure 9 and Figure 10 for each given initial magnetic field strength (represented in log). For each fraction shown, the corresponding period is the minimum value achieved by that fraction of cases. Of the three velocities, the largest spin period at a given fraction is recorded. In the last row, we include the largest spin rates for each magnetic field strength.

≥ 10 kyr, the only torque is due to magnetic dipole emission, which does not affect the long-term evolution of pulsars if the period is already very long. With this in mind, we look at the $P - \dot{P}$ evolution over time for these pulsars, as plotted by Figure 12. For the strongest initial magnetic fields, we observe NSs with spin periods $10^2 \sim 10^3$ s within one year. By 100 years, a larger

fraction of the NS population (particularly those with initial B-fields $\geq 10^{14}$ G) reaches spin periods $> 10^2$ s.

The NSs in our model experience high \dot{P} values within their first year of evolution. This can be understood to be due to a combination of magnetic dipole emission and the NSs entering the propeller phase, where they undergo rapid spin-down as their spin periods reach their equilibrium periods. After $\gtrsim 10^4$ years, \dot{P} is very low

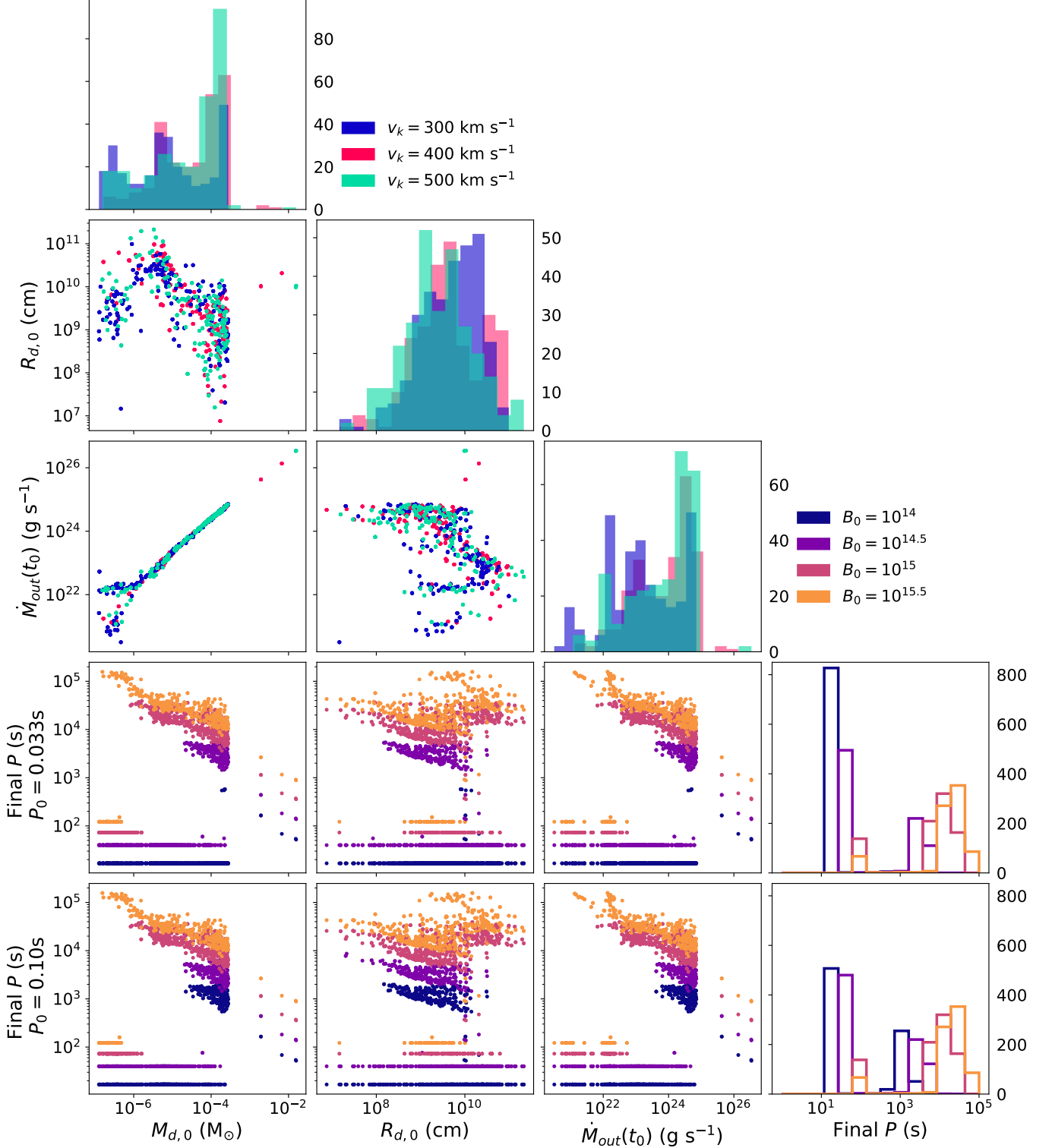


Figure 11. Corner plot of initial disk parameters and final spin periods. We separate the final spin period results by initial period. Colors of plots involving the spin periods indicate initial B-field strength and are for all kick velocities that we tested. Other plots not involving the final spin periods are separated by initial kick velocity. $M_{d,0}$ indicates the total captured mass, $R_{d,0}$ is the initial circularization radius, and \dot{M}_{out} is the outer disk accretion rate at $t_0 = 20$ hrs.

as it is only caused by magnetic dipole emission, which provides little torque on the NSs (given the long period and weakened field strength).

7. DISCUSSION

In this section, we compare our results to observations, and then we discuss the limitations of our model as well as the broader implications that are not studied in detail in this work.

7.1. Comparison to Observations

Current observations of pulsars and ULPs suggest that there might be a bimodal distribution in the period distribution — canonical pulsars have spin periods ≤ 12 s and ULPs have periods of minutes to hours. However, we note that no statistical study has been done to definitely show the bimodal distribution predicted in this work. These two distinct groups of periods may be due to observational biases, and in the upcoming years there may be more radio pulsators discovered with intermediate spin periods. In our model (and in fact all ULP models based on NSs spinning down due to a propeller phase), the period distribution is bimodal for the following reason. A NS either never interacts with its accretion disk (in case of weak initial magnetic fields and low disk masses) and evolves as a canonical NS with a fast spin, or once the NS magnetosphere interacts with the accretion disk, the system enters the propeller phase where the NS is rapidly spun-down to very long periods of 10^2 s up to 10^5 s. We encourage a future statistical study to demonstrate or rule out such a bimodal distribution of spin periods in the current sample of pulsars and ULPs.

In terms of individual spin periods, our model predicts short ULPs, such as PSR J0901-4046 with $P = 76$ s (M. Caleb et al. 2022), which are produced even for relatively low initial magnetic field strengths 10^{13} G, as long as the initial periods are sufficiently long $P_0 \gtrsim 0.1$ s (such that the system enters the propeller phase). Within our model, such short ULPs are produced for initial field strengths up to $10^{14.5}$ G. On the other hand, the longest ULPs, such as IE-1613 with $P = 6.7$ hrs (A. De Luca et al. 2006), are only produced for relatively strong initial field strengths of $B_0 \gtrsim 10^{15}$ G — consistent with typical magnetars.

Our model also can explain the upper limits of period derivative for the observed ULPs. During the propeller phase, the period derivative becomes extremely large \dot{P} up to 10^{-5} , which is easily measurable. However, since the propeller phase is extremely short-lived (lasting for decades), it is difficult to catch the evolution observationally. Once the NS reaches the equilibrium spin, then the period changes on the disk evolutionary timescales of 1 to 10 kyr, which gives rise to

$\dot{P} \sim 10^{-9}$ to 10^{-7} (10^3 s to 10^5 s divided by 10 kyr). However, during the equilibrium-spin phase, the signatures of the accretion disk may still be detectable, e.g., in the form of mid-infrared emission from the X-ray-heated disk. The infrared emission from the outer disk has luminosity (Equation 10) and effective temperature

$$\begin{aligned} L_{\text{IR}} &\simeq 3 \times 10^{32} \text{ erg s}^{-1} \frac{L_x}{10^{35} \text{ erg s}^{-1}} \frac{H/R_d}{0.03}, \\ T_{\text{IR}} &\simeq 250 \text{ K} \left(\frac{L_x}{10^{35} \text{ erg s}^{-1}} \frac{H/R_d}{0.03} \right)^{1/4} \left(\frac{R_d}{\text{AU}} \right)^{-1/2}, \end{aligned} \quad (29)$$

where L_x is the X-ray luminosity of the neutron star, $H/R_d \sim 3\%$ is the typical aspect ratio in our model, and R_d is the outer disk radius. More observational and theoretical works along this direction are needed to see if the disk signatures are observable. On longer timescales $t \gtrsim 10$ kyr (which is the case for most observed systems), the disks either evaporate or become inactive. In this case, the NS spin-down is only due to magnetic dipole emission, which produces a very low period-derivative $\dot{P} \sim 10^{-18} (P/10^3 \text{ s})^{-1} (B/10^{12} \text{ G})^2$, which are not detectable for ULPs. In our model, the observed ULPs are consistent with relatively old systems where the disks have become inactive. Future observations may detect the more rare cases in the equilibrium-spin phase with much larger \dot{P} .

We additionally discuss the formation rate of ULPs. In the following, we calculate our rates under the assumption that ULPs require magnetar-level initial field strengths $B_0 \gtrsim 10^{14}$ G (although some short ULPs may be produced with B_0 as low as 10^{13} G).

We start from the core-collapse rate of 3 per century in our Galaxy (E. F. Keane & M. Kramer 2008, and cites therein) and assume that a fraction $f_{\text{mag}} \sim 10\%$ of NSs are formed as magnetars (although this fraction could be larger, e.g., P. Beniamini et al. 2019; R. Gill & J. Heyl 2007; E. F. Keane & M. Kramer 2008). Based on the rate of type-Ib/c supernovae (e.g., I. Shivvers et al. 2017), we assume that 30% of NSs are born in a close binary as studied in this work. If magnetar formation are not correlated with stripped-envelope supernovae, we obtain a formation rate of magnetars born in stripped-envelope systems to be of the order 10^{-3} yr^{-1} in our Galaxy.

As shown in Figs. 9 and 10, we find the fractional outcome of ULPs with $P \gtrsim 10^3$ s to be $f_{\text{ULP}} \sim 3\%$ to 10% , considering different kick velocities, initial magnetic field strengths, and initial NS spin periods. In this work, we only consider a pre-supernova binary separation of $20 R_{\odot}$, which corresponds to orbital period $P_{\text{orb}} \simeq 3$ d. We expect the occurrence fraction of ULPs

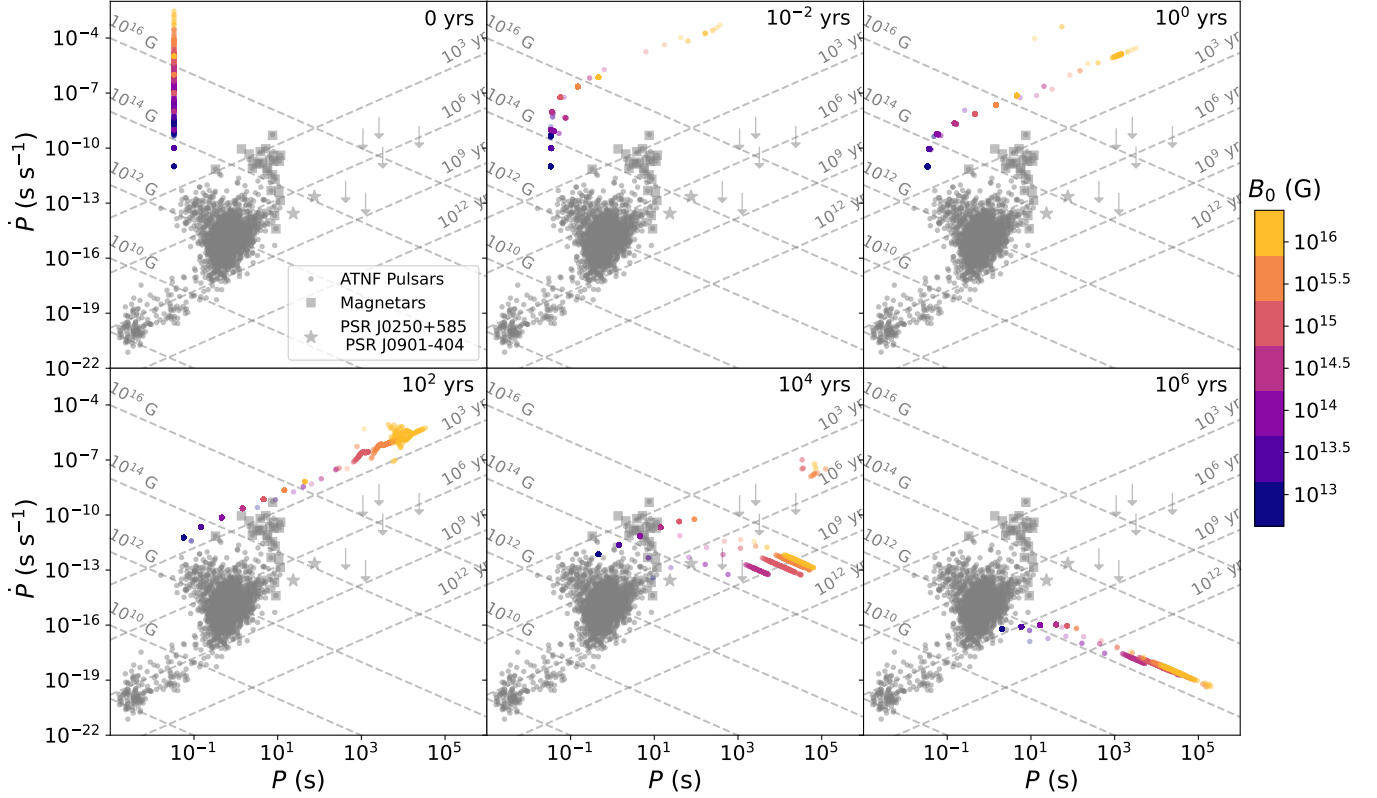


Figure 12. $P-\dot{P}$ Diagram over time. Colored points indicates initial B-field strength of our simulated NSs. Plotted additionally in gray are pulsars from the ATNF catalog (R. N. Manchester et al. 2005, <http://www.atnf.csiro.au/research/pulsar/psrcat>), magnetars (S. A. Olausen & V. M. Kaspi 2014, <http://www.physics.mcgill.ca/~pulsar/magnetar/main.html>), and long period pulsars PSR J0250 and PSR J0901 (C. M. Tan et al. 2018; M. Caleb et al. 2022). Other recently discovered long period radio transients are indicated by downwards arrows to show their upper limits (F. A. Dong et al. 2024; N. Hurley-Walker et al. 2022, 2023; M. Caleb et al. 2024; A. De Luca et al. 2006). Lines of equal B-field strength are calculated from spin-down due to magnetic dipole radiation: $\dot{P} = (4\pi^2 B)^2 / (3Ic^3 P)$. Lines of equal age are calculated using the spin-down assuming magnetic braking: $\dot{P} = P / (2\tau)$, where τ is the characteristic age. Although this figure is for NSs with $P_0 = 0.033$ s, for $B_0 \geq 10^{14}$ G, our results do not significantly change. We keep our plot within reasonable margins of what has been observed by current pulsars.

to increase for shorter orbital periods for various reasons. A larger fraction of the ejecta would be intercepted by the companion star, the companion star is more strongly modified by a larger ram pressure, and a shorter orbital separation also increases the chance of closer encounters between the NS and companion star. Thus, we estimate the ULP formation rate to be

$$\dot{N}_{\text{ULP}} \sim 10^{-4} \text{ yr}^{-1} \frac{f_{\text{ULP}}}{10\%} \frac{f_{\text{mag}}}{10\%}, \quad (30)$$

where f_{ULP} is the fractional outcomes of ULPs from magnetars born in close binary systems and f_{mag} is the magnetar fraction. If all NSs are able to emit radio emission for up to $t_{\text{life}} \sim 1$ Myr, then the total number of radio-bright ULPs in the Milky Way is given by $N_{\text{ULP}} \sim 10^2$ for our fiducial values in eq. (30).

Note that our estimate suffers from a number of major uncertainties that are beyond the scope of this work: (1) the magnetar formation rate may be higher than

$f_{\text{mag}} \sim 10\%$ (P. Beniamini et al. 2019, whose population study prefers $f_{\text{mag}} \sim 40\%$); (2) if stripped-envelope supernovae preferentially make magnetars (due to e.g., faster core rotation from tidal spin-up in binary interactions, J. Fuller & W. Lu 2022), one may effectively take $f_{\text{mag}} \sim 100\%$ within the stripped-envelope supernova population; and (3) the radio emission lifetime for ULPs (arbitrarily taken to be 1 Myr in the above estimate) is unknown, although the lack of bright persistent X-ray emission from the observed ULPs may suggest that they are likely much older than the known Galactic magnetar population whose typical ages are 1–10 kyrs. If we factor in all these uncertainties (while keeping $t_{\text{life}} \sim 1$ Myr), we find $10 \lesssim N_{\text{ULP}} \lesssim 10^3$. In the most optimistic case of $N_{\text{ULP}} \sim 10^3$, the nearest ULP may be as close as 300 pc away from the solar system.

Despite the uncertainties, we conclude that our model should contribute a non-negligible fraction of observable ULPs in the Milky Way.

7.2. Limitations

In this subsection, we discuss the limitations of our model, which may be improved in future works.

First, our model can be improved by considering a radially resolved disk (instead of a one-zone model) and a more physical consideration for evaporation. This would allow us to capture the radial dependence of irradiation and evaporation — this is important to capture the final fate of the NS and the disk.

Second, our mass capture estimates are also limited by the set-up of the hydrodynamic simulation. We do not consider the realistic mass capture by the gravitational potential of a NS moving in an unbound trajectory, as it is more computational heavy to do so. Moreover, the captured slow-moving gas near the center of explosion is considered as a part of “fallback accretion” and hence removed from our disk modeling (as described in § 4). This is because the gas near the explosion center is likely not properly modeled by our $\gamma = 5/3$ equation of state and our initial conditions are also likely simplistic. This makes our mass capture estimates conservative — it is possible that fallback accretion also contributes to disk formation and that a larger fraction of NSs evolve into ULPs.

Third, we do not survey a broad parameter space in companion star masses and orbital separations. We expect our results, especially the fractional outcome of ULPs, to depend strongly on the orbital separation. This is mainly because (1) the ram pressure p_{ram} of the ejecta at the position of the companion star scales with the orbital separation a_{sep} as $p_{\text{ram}} \propto a_{\text{sep}}^{-3}$ and (2) the solid angle Ω_* spanned by the companion star (of a given radius) scales with the orbital separation as $\Omega_* \propto a_{\text{sep}}^{-2}$. For these reasons, we expect the fractional outcome of ULPs to increase for shorter orbital separations. Unfortunately, the pre-supernova orbital separations of stripped-envelope supernovae are currently highly uncertain.

7.3. Other Consequences

In this subsection, we briefly mention other consequences of our model that are not directly related to ULPs.

Although in this paper we only consider unbound orbits, observations and binary population synthesis models suggest that about 5% (or higher) of the time a neutron star will remain bound to its companion post core-collapse (e.g., A. A. Chrimes et al. 2022). If the NS remains bound to the companion, it will repetitively pass through the companion’s inflated envelope (see Figure 1) and hence produce periodic power injections into the supernova ejecta as suggested by R. Hirai & P. Podsiad-

lowski (2022). This can potentially explain a recently discovered stripped-envelope supernova, SN 2022jli (P. Chen et al. 2024). SN 2022jli showed a 12.4-day periodicity in its brightness variations and H α velocities (P. Chen et al. 2024); this periodicity is likely caused by the remnant compact object being in a bound orbit with its companion post supernova. SN 2015ap also showed possible modulations in its light curve with a 8.4 day periodicity that could similarly be described by binary interactions (F. Ragosta et al. 2025).

If magnetars form in close binaries, our work shows that a fraction ($\sim 10\%$, depending on the orbital period) of them are born with accretion disks. An accretion disk could explain the excess infrared emission from magnetars, such as 4U 0142+61 and 1E 2259+586 (F. Hulleman et al. 2004; Z. Wang et al. 2006; Ü. Ertan et al. 2007; D. L. Kaplan et al. 2009). As more infrared observations are made on magnetars (e.g., J. Hare et al. 2024), we may be able to constrain the percentage of magnetars that have accretion disks and compare it to our predictions. Furthermore, there have been multiple planets found orbiting pulsars (e.g., A. Wolszczan & D. A. Frail 1992). Our work can be used to determine if the disk contains sufficient mass and angular momentum to form such exoplanets.

8. SUMMARY

In this paper, we propose that a neutron star born in a close binary system can acquire an accretion disk by interacting with the companion star’s shock-inflated envelope. We focus on the cases where the neutron star becomes unbound from the binary due to a natal kick. We follow the long-term disk evolution and its interaction with the neutron star’s magnetosphere. These neutron stars may be observed as isolated pulsars whose spin periods are affected by the additional torque from the accretion disk. Our results are summarized as follows:

1. At a pre-supernova binary separation of $20 R_{\odot}$ (or orbital period 3 days), we find that the neutron star becomes isolated with a surrounding accretion disk 8-10% of the time. We expect the disk formation probability to increase towards closer binary separations.
2. The disks formed in our simulation have captured masses in the range $10^{-7} \sim 10^{-2} M_{\odot}$, initial angular momentum of $10^{44} \sim 10^{49}$ erg s, and initial circularization radii of $10^6 \sim 10^{11}$ cm. Compared to possible disk formation from supernova fallback, our binary model provides a new channel for disk formation with higher angular momenta.

3. We find that long-term interactions between the accretion disk and the neutron star's magnetosphere lead to a bimodal distribution of spin periods. The majority of neutron stars born in close binaries belong to the short-period mode with $P \lesssim 12$ s because their spins have not been affected by the accretion disk. A minority (roughly 1% to 10%) of neutron stars born in close binaries evolve to the long-period mode with $P \gtrsim 10^3$ s as a result of a short-lived propeller phase which occurs almost exclusively for initial magnetic field strengths of $B_0 \gtrsim 10^{14}$ G — typical for magnetars in the Milky Way. The long-period mode is consistent with observed ULPs such as CHIME J0630+25, GLEAM-J1627, ASKAP-J1935, and IE 161348-505, provided that these objects initially had magnetar-level field strengths and underwent a propeller phase in their evolution. A small fraction (0.1% to 1%) of pulsars with moderate $10^{13} \lesssim B_0 \lesssim 10^{14}$ G and relatively slow initial periods $P_0 \gtrsim 0.1$ s evolve to $P \sim 10^2$ s (similar to PSR J0901-4046) and fill in the gap between the two period modes.
4. We find that longer periods are produced for stronger initial field strengths: $P \sim 10^4$ s requires $B_0 \sim 10^{14.5}$ G, $P \sim 10^5$ s requires $B_0 \sim 10^{15}$ G, and only magnetars with $B_0 \gtrsim 10^{15}$ G evolve to the longest periods $P \gtrsim 10^5$ s. This is because, soon after the system enters the propeller phase, the neutron star reaches the equilibrium spin $P_{\text{eq}} \propto B^{6/7}$ (Equation 26).
5. We predict a ULP formation rate of $\dot{N}_{\text{ULP}} \sim 10^{-4}$ yr for our fiducial parameters (eq. 30), but a broad range of $10^{-5} \lesssim \dot{N}_{\text{ULP}} \lesssim 10^{-3}$ yr $^{-1}$ is allowed. Thus, the total number of ULPs with $P \gtrsim 10^3$ s in the Milky Way is in the range of $10 \lesssim N_{\text{ULP}} \lesssim 10^3$ for an active lifetime of 1 Myr. The main uncertainties in our estimate are (1) the magnetar fraction of neutron stars born in close binaries ($10\% \lesssim f_{\text{mag}} \lesssim 100\%$), and (2) the occurrence fraction of disks (f_{disk}). We find that $f_{\text{disk}} \sim 10\%$ for a pre-supernova separation of $20 R_\odot$, but it depends sensitively on separation.
6. On a timescale of 10 kyrs, once the accretion disk evaporates (due to X-ray irradiation) or becomes inactive (due to mid-plane temperature $T \lesssim 10^2$ K), we predict that the period derivatives of ULPs drops to very small values $\dot{P} \lesssim 10^{-18}$ that

are not detectable by current observations. However, there is a small population of magnetars younger than 10 kyrs with active disk interactions, and in these cases, we predict detectable period derivatives of $10^{-9} \lesssim \dot{P} \lesssim 10^{-7}$, because the neutron star is kept at the equilibrium spin rate as the disk evolves.

7. The X-ray irradiation of the disk produces mid-infrared emission with $L_{\text{IR}} \sim 10^{32}$ erg s $^{-1}$ and typical effective temperature $T_{\text{IR}} \sim 250$ K for the outer disk. The mid-infrared emission only lasts for a relatively short duration of ~ 10 kyr.
8. We also predict that, for bound post-supernova orbits, the neutron star will periodically pass through the shock-inflated envelope of the companion star and that the accretion power may produce brightened, periodically modulated emission following a type-Ib/c supernova. This model may potentially explain the peculiar properties of SN2023jli (P. Chen et al. 2024).

ACKNOWLEDGMENTS

We thank Bruce Grossan, J. J. Eldridge, and Ping Chen for useful conversations. The research of S.C. and W.L. was supported by the Hellman Fellows Fund. This research benefited from interactions at workshops funded by the Gordon and Betty Moore Foundation through grant GBMF5076 and through interactions at the Kavli Institute for Theoretical Physics, supported by NSF PHY-2309135. C. L. acknowledges support from the Miller Institute for Basic Research at UC Berkeley. T.L.S.W. acknowledges support from the Gordon and Betty Moore Foundation through grant GBMF5076. This research used the Savio computational cluster resource provided by the Berkeley Research Computing program at the University of California, Berkeley (supported by the UC Berkeley Chancellor, Vice Chancellor for Research, and Chief Information Officer). This research used resources of the National Energy Research Scientific Computing Center (NERSC), a Department of Energy User Facility (project m2218-2025).

Software: ATHENA++ (J. M. Stone et al. 2020), numpy (C. R. Harris et al. 2020), scipy (P. Virtanen et al. 2020), matplotlib (J. D. Hunter 2007)

APPENDIX

A. RESOLUTION TESTS

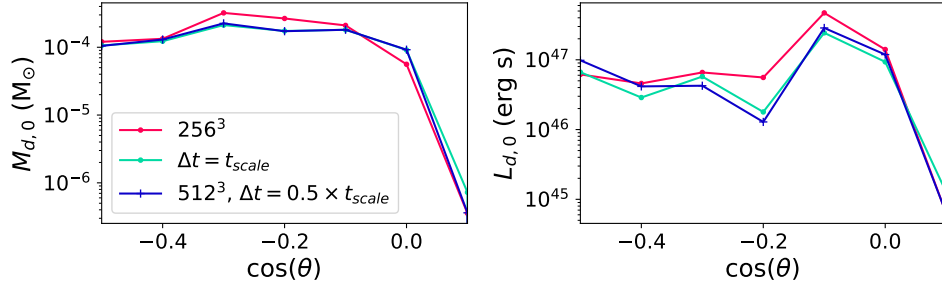


Figure 13. Time and spatial resolution tests. We consider kicks in the $\cos(\varphi_k) = 1.0$ plane for $v_k = 400 \text{ km s}^{-1}$ as an example, and show the total mass and angular momentum captures for each angle $\theta = \pi/2 - \theta_k$. Angles not included either are bound orbit trajectories or resulted in negligible mass capture.

In this section, we describe our convergence tests on the spatial and time resolutions of our simulations.

First, we run another simulation with the same parameters as described in §3, except we decrease the spatial resolution to a grid size of 256^3 to compare to our original 512^3 grid. Using the same Bondi capture methods described in §4, we compare the captured mass and angular momentum between the two grid sizes.

Secondly, for our original simulation on a 512^3 grid, we decrease the time in between each 3D snapshot data dump to test the time resolution of our Bondi mass capture method. As described in §4, our fiducial 3D snapshot dump is once every $\delta t = 0.5 \times t_{\text{scale}}$. We double the time interval between each snapshot dump and run our Bondi mass capture as described in §4.

The convergence of our results are demonstrated in Figure 13.

B. DISK X-RAY HEATING

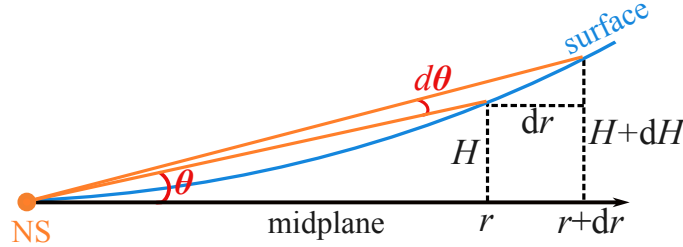


Figure 14. Geometry for disk heating in the case of a point-source.

In this section, we derive the incident flux on the surface of a flared disk by treating the NS as a point source. We assume that the scale height of the disk scales with radius as a power-law $H \propto r^n$, with $n = d \ln H / d \ln r$. Let θ be the angle of the disk surface from the mid-plane (see Figure 14), with $\tan \theta = H/r$. The solid angle spanned by the annulus from r to $r + dr$ is $d\Omega = 2\pi \cos \theta d\theta$, and

$$d\theta = \cos^2 \theta d(H/r) = \cos^2 \theta \frac{H}{r^2} (n-1) dr. \quad (\text{B1})$$

The corresponding differential disk surface area is

$$dA = 2\pi r \sqrt{(dH)^2 + (dr)^2} = 2\pi r dr \sqrt{1 + n^2 \tan^2 \theta}. \quad (\text{B2})$$

Thus, the flux per unit surface area of the disk is

$$F(r) = \frac{L d\Omega / 4\pi}{dA} = \frac{L}{4\pi r^2} \frac{H}{r} \frac{\cos^3 \theta (n-1)}{\sqrt{1 + n^2 \tan^2 \theta}}. \quad (\text{B3})$$

At sufficiently late time ($t \gtrsim 1$ week), we find $\theta \sim H/r \ll 1$ and hence

$$F(r) \approx \frac{L}{4\pi r^2} \frac{H}{r} (n-1), \quad (\text{B4})$$

Depending on the regime the disk is in, there are several solutions to n . For example, [E. I. Chiang & P. Goldreich \(1997\)](#) finds a value of $9/7$ for a passive disk, whereas [J. Frank & A. King \(2002\)](#) provided $n = 9/8$ for an accreting disk with viscous dissipation under the Kramer’s opacity scaling law. We taken an intermediate value of $n = 6/5$ in this work.

C. VISCOSITY DEPENDENCY

Our disk evolution model adopts a varying viscosity parameter α that transitions from the hot regime $\alpha_{\text{hot}} = 0.1$ to the cold regime $\alpha_{\text{cold}} = 0.02$. In Figure 15, we show the final period distribution for constant $\alpha = 0.02$ and $\alpha = 0.1$ (all else are kept the same). We find that the results in our default model are very similar to the case with a constant $\alpha = 0.02$. As for the constant $\alpha = 0.1$ case, the results are still qualitatively similar in that ULPs can still form but with a slightly lower rate.

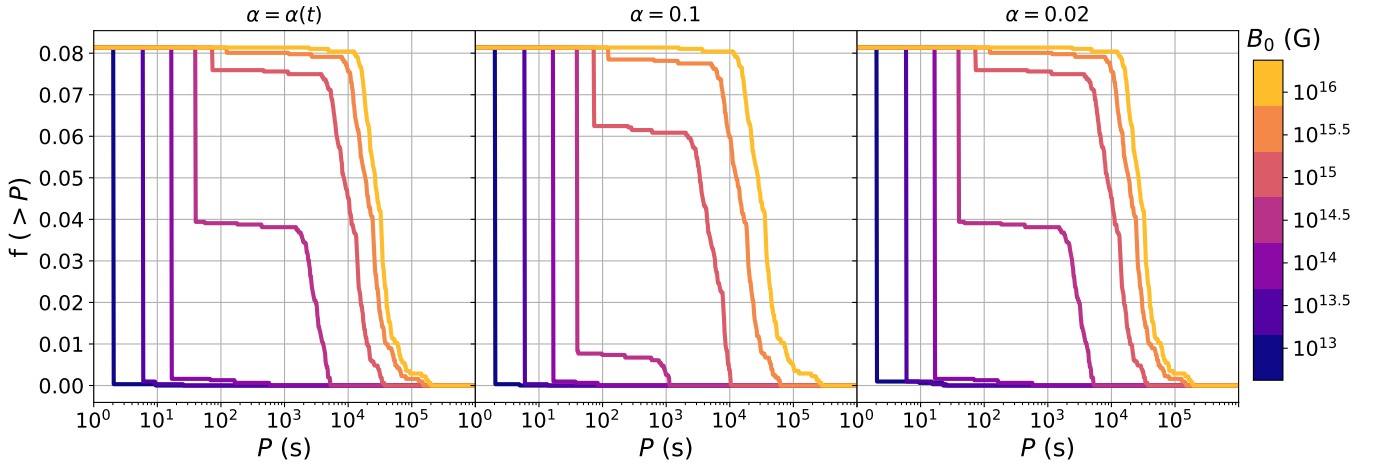


Figure 15. Final period distributions for different α models. We fix $v_k = 400 \text{ km s}^{-1}$ and $P_0 = 0.033 \text{ s}$. $\alpha(t)$ corresponds to the default model in Equation (7).

D. B-FIELD DECAY DEPENDENCY

We also considered a different field decay model as described in [D. N. Aguilera et al. \(2008\)](#). In their model, the magnetic field evolves according to timescales of $\tau_{\text{Hall}} = 4\pi n_e L^2 / c B_0$ for the Hall effect, and $\tau_{\text{Ohm}} = 4\pi \sigma L^2 / c^2$ for ohmic dissipation, where e is the electron charge, n_e is the average electron density in the crust, σ is the conductivity, and L is the scale length for the crust. Using the prescription in [M. Ronchi et al. \(2022\)](#), we take $n_e = 10^{35} \text{ cm}^{-3}$, $L = 1 \text{ km}$, and $\sigma = 10^{24} \text{ s}^{-1}$, leaving us with $\tau_{\text{Hall}} \sim 6.4 \times 10^4 \text{ yr } B_{0,14}^{-1}$ and $\tau_{\text{Ohm}} \sim 4.4 \times 10^6 \text{ yr}$ (with $B_{0,14} = B_0 / 10^{14} \text{ G}$). The magnetic field decay is dominated by τ_{Hall} at earlier times and by τ_{Ohm} at later times, as follows:

$$B(t) = B_0 \frac{e^{-t/\tau_{\text{Ohm}}}}{1 + \frac{\tau_{\text{Ohm}}}{\tau_{\text{Hall}}} [1 - e^{-t/\tau_{\text{Hall}}}]}. \quad (\text{D5})$$

The final spin period distributions for different field decay prescriptions are shown in Figure 16. The similarity of the results means that our conclusions are not very sensitive to the field decay models considered in the literature, and this is mainly because the propeller phase usually occurs within the first 1 kyrs of evolution before the magnetic fields decay substantially.

REFERENCES

- Aguilera, D. N., Pons, J. A., & Miralles, J. A. 2008, *ApJL*, 673, L167, doi: [10.1086/527547](https://doi.org/10.1086/527547)
- Alpar, M. A., Çalıřkan, ř., & Ertan, Ü. 2013, in *IAU Symposium*, Vol. 290, Feeding Compact Objects: Accretion on All Scales, ed. C. M. Zhang, T. Belloni, M. Méndez, & S. N. Zhang, 93–100, doi: [10.1017/S1743921312019291](https://doi.org/10.1017/S1743921312019291)

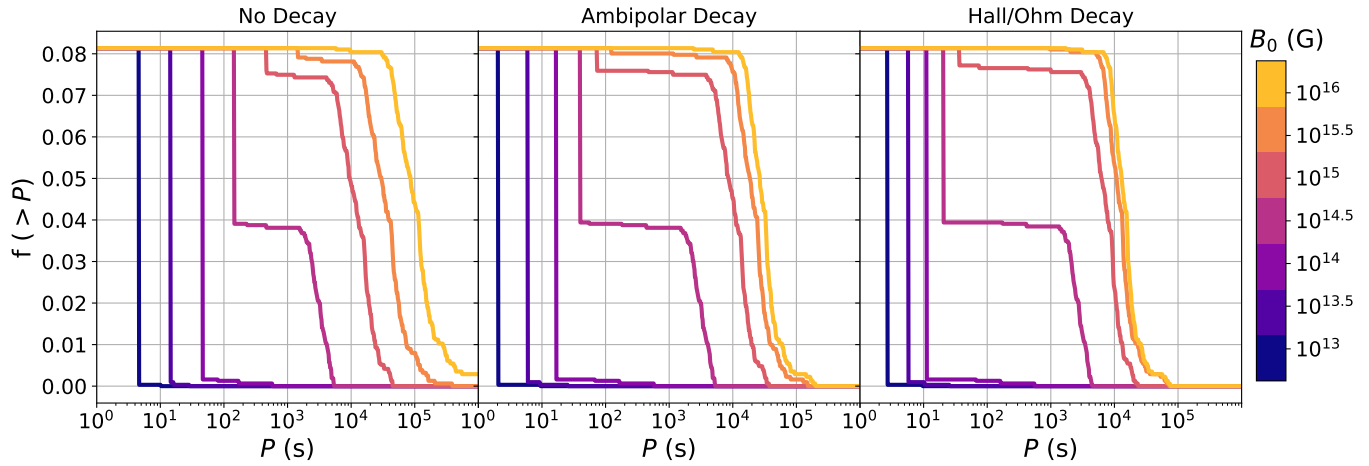


Figure 16. Final period distributions for different field decay models. We fix $v_k = 400 \text{ km s}^{-1}$ and $P_0 = 0.033 \text{ s}$.

- Barbarino, C., Sollerman, J., Taddia, F., et al. 2021, *A&A*, 651, A81, doi: [10.1051/0004-6361/202038890](https://doi.org/10.1051/0004-6361/202038890)
- Bauer, E. B., White, C. J., & Bildsten, L. 2019, *The Astrophysical Journal*, 887, 68, doi: [10.3847/1538-4357/ab4ea4](https://doi.org/10.3847/1538-4357/ab4ea4)
- Begelman, M. C., McKee, C. F., & Shields, G. A. 1983, *ApJ*, 271, 70, doi: [10.1086/161178](https://doi.org/10.1086/161178)
- Beniamini, P., Hotokezaka, K., van der Horst, A., & Kouveliotou, C. 2019, *MNRAS*, 487, 1426, doi: [10.1093/mnras/stz1391](https://doi.org/10.1093/mnras/stz1391)
- Beniamini, P., Wadiasingh, Z., Hare, J., et al. 2023, *MNRAS*, 520, 1872, doi: [10.1093/mnras/stad208](https://doi.org/10.1093/mnras/stad208)
- Blandford, R. D., & Begelman, M. C. 1999, *MNRAS*, 303, L1, doi: [10.1046/j.1365-8711.1999.02358.x](https://doi.org/10.1046/j.1365-8711.1999.02358.x)
- Bondi, H. 1952, *MNRAS*, 112, 195, doi: [10.1093/mnras/112.2.195](https://doi.org/10.1093/mnras/112.2.195)
- Bondi, H., & Hoyle, F. 1944, *MNRAS*, 104, 273, doi: [10.1093/mnras/104.5.273](https://doi.org/10.1093/mnras/104.5.273)
- Caleb, M., Heywood, I., Rajwade, K., et al. 2022, *Nature Astronomy*, 6, 828, doi: [10.1038/s41550-022-01688-x](https://doi.org/10.1038/s41550-022-01688-x)
- Caleb, M., Lenc, E., Kaplan, D. L., et al. 2024, *Nature Astronomy*, doi: [10.1038/s41550-024-02277-w](https://doi.org/10.1038/s41550-024-02277-w)
- Camilo, F., Ransom, S. M., Halpern, J. P., et al. 2006, *Nature*, 442, 892, doi: [10.1038/nature04986](https://doi.org/10.1038/nature04986)
- Chen, H.-P., Rau, S.-J., & Pan, K.-C. 2023, *ApJ*, 949, 121, doi: [10.3847/1538-4357/acc9af](https://doi.org/10.3847/1538-4357/acc9af)
- Chen, K., & Ruderman, M. 1993, *ApJ*, 402, 264, doi: [10.1086/172129](https://doi.org/10.1086/172129)
- Chen, P., Gal-Yam, A., Sollerman, J., et al. 2024, *Nature*, 625, 253, doi: [10.1038/s41586-023-06787-x](https://doi.org/10.1038/s41586-023-06787-x)
- Chevalier, R. A., & Soker, N. 1989, *ApJ*, 341, 867, doi: [10.1086/167545](https://doi.org/10.1086/167545)
- Chiang, E. I., & Goldreich, P. 1997, *ApJ*, 490, 368, doi: [10.1086/304869](https://doi.org/10.1086/304869)
- Cho, H., Prather, B. S., Su, K.-Y., Narayan, R., & Natarajan, P. 2024, *ApJ*, 977, 200, doi: [10.3847/1538-4357/ad9561](https://doi.org/10.3847/1538-4357/ad9561)
- Chrimes, A. A., Levan, A. J., Fruchter, A. S., et al. 2022, *MNRAS*, 513, 3550, doi: [10.1093/mnras/stac1090](https://doi.org/10.1093/mnras/stac1090)
- Coleman, M. S. B., Blaes, O., Hirose, S., & Hauschildt, P. H. 2018, *ApJ*, 857, 52, doi: [10.3847/1538-4357/aab6a7](https://doi.org/10.3847/1538-4357/aab6a7)
- Davidson, K., & Ostriker, J. P. 1973, *ApJ*, 179, 585, doi: [10.1086/151897](https://doi.org/10.1086/151897)
- De Luca, A., Caraveo, P. A., Mereghetti, S., Tiengo, A., & Bignami, G. F. 2006, *Science*, 313, 814, doi: [10.1126/science.1129185](https://doi.org/10.1126/science.1129185)
- de Ruiter, I., Rajwade, K. M., Bassa, C. G., et al. 2024, *arXiv e-prints*, arXiv:2408.11536, doi: [10.48550/arXiv.2408.11536](https://doi.org/10.48550/arXiv.2408.11536)
- Dong, F. A., Clarke, T., Curtin, A. P., et al. 2024, *arXiv e-prints*, arXiv:2407.07480, doi: [10.48550/arXiv.2407.07480](https://doi.org/10.48550/arXiv.2407.07480)
- Drout, M. R., Soderberg, A. M., Gal-Yam, A., et al. 2011, *ApJ*, 741, 97, doi: [10.1088/0004-637X/741/2/97](https://doi.org/10.1088/0004-637X/741/2/97)
- Duchêne, G., & Kraus, A. 2013, *ARA&A*, 51, 269, doi: [10.1146/annurev-astro-081710-102602](https://doi.org/10.1146/annurev-astro-081710-102602)
- Ekşi, K. Y., Hernquist, L., & Narayan, R. 2005, *ApJL*, 623, L41, doi: [10.1086/429915](https://doi.org/10.1086/429915)
- Eldridge, J. J., Fraser, M., Smartt, S. J., Maund, J. R., & Crockett, R. M. 2013, *MNRAS*, 436, 774, doi: [10.1093/mnras/stt1612](https://doi.org/10.1093/mnras/stt1612)
- Enoto, T., Sasano, M., Yamada, S., et al. 2014, *ApJ*, 786, 127, doi: [10.1088/0004-637X/786/2/127](https://doi.org/10.1088/0004-637X/786/2/127)
- Ertan, Ü., Ekşi, K. Y., Erkut, M. H., & Alpar, M. A. 2009, *ApJ*, 702, 1309, doi: [10.1088/0004-637X/702/2/1309](https://doi.org/10.1088/0004-637X/702/2/1309)
- Ertan, Ü., Erkut, M. H., Ekşi, K. Y., & Alpar, M. A. 2007, *ApJ*, 657, 441, doi: [10.1086/510303](https://doi.org/10.1086/510303)

- Ertl, T., Woosley, S. E., Sukhbold, T., & Janka, H. T. 2020, *ApJ*, 890, 51, doi: [10.3847/1538-4357/ab6458](https://doi.org/10.3847/1538-4357/ab6458)
- Esposito, P., De Luca, A., Turolla, R., et al. 2019, *A&A*, 626, A19, doi: [10.1051/0004-6361/201935412](https://doi.org/10.1051/0004-6361/201935412)
- Fan, Y.-N., Xu, K., & Chen, W.-C. 2024, *ApJ*, 967, 24, doi: [10.3847/1538-4357/ad3aef](https://doi.org/10.3847/1538-4357/ad3aef)
- Ferguson, J. W., Alexander, D. R., Allard, F., et al. 2005, *ApJ*, 623, 585, doi: [10.1086/428642](https://doi.org/10.1086/428642)
- Frank, J., & King, A. 2002, *Accretion Power in Astrophysics: Third Edition* (Cambridge, UK: Cambridge University Press)
- Fuller, J., & Lu, W. 2022, *MNRAS*, 511, 3951, doi: [10.1093/mnras/stac317](https://doi.org/10.1093/mnras/stac317)
- Gagliano, A., Izzo, L., Kilpatrick, C. D., et al. 2022, *ApJ*, 924, 55, doi: [10.3847/1538-4357/ac35ec](https://doi.org/10.3847/1538-4357/ac35ec)
- Gençali, A. A., Ertan, Ü., & Alpar, M. A. 2022, *MNRAS*, 513, L68, doi: [10.1093/mnrasl/slac034](https://doi.org/10.1093/mnrasl/slac034)
- Gençali, A. A., Ertan, Ü., & Alpar, M. A. 2023, *MNRAS*, 520, L11, doi: [10.1093/mnrasl/slac164](https://doi.org/10.1093/mnrasl/slac164)
- Ghosh, P., & Lamb, F. K. 1978, *ApJL*, 223, L83, doi: [10.1086/182734](https://doi.org/10.1086/182734)
- Gill, R., & Heyl, J. 2007, *MNRAS*, 381, 52, doi: [10.1111/j.1365-2966.2007.12254.x](https://doi.org/10.1111/j.1365-2966.2007.12254.x)
- Goldreich, P., & Reisenegger, A. 1992, *ApJ*, 395, 250, doi: [10.1086/171646](https://doi.org/10.1086/171646)
- Gudmundsson, E. H., Pethick, C. J., & Epstein, R. I. 1982, *ApJL*, 259, L19, doi: [10.1086/183840](https://doi.org/10.1086/183840)
- Guo, M., Stone, J. M., Quataert, E., & Kim, C.-G. 2024, *ApJ*, 973, 141, doi: [10.3847/1538-4357/ad5fe7](https://doi.org/10.3847/1538-4357/ad5fe7)
- Hameury, J.-M., Menou, K., Dubus, G., Lasota, J.-P., & Hure, J.-M. 1998, *MNRAS*, 298, 1048, doi: [10.1046/j.1365-8711.1998.01773.x](https://doi.org/10.1046/j.1365-8711.1998.01773.x)
- Han, J. L., Wang, C., Wang, P. F., et al. 2021, *Research in Astronomy and Astrophysics*, 21, 107, doi: [10.1088/1674-4527/21/5/107](https://doi.org/10.1088/1674-4527/21/5/107)
- Hare, J., Pavlov, G. G., Posselt, B., et al. 2024, *ApJ*, 972, 176, doi: [10.3847/1538-4357/ad5ce5](https://doi.org/10.3847/1538-4357/ad5ce5)
- Harris, C. R., Millman, K. J., van der Walt, S. J., et al. 2020, *Nature*, 585, 357, doi: [10.1038/s41586-020-2649-2](https://doi.org/10.1038/s41586-020-2649-2)
- Hinkle, K. H., Lebzelter, T., Fekel, F. C., et al. 2020, *ApJ*, 904, 143, doi: [10.3847/1538-4357/abbe01](https://doi.org/10.3847/1538-4357/abbe01)
- Hirai, R., & Podsiadlowski, P. 2022, *MNRAS*, 517, 4544, doi: [10.1093/mnras/stac3007](https://doi.org/10.1093/mnras/stac3007)
- Hirai, R., Podsiadlowski, P., & Yamada, S. 2018, *ApJ*, 864, 119, doi: [10.3847/1538-4357/aad6a0](https://doi.org/10.3847/1538-4357/aad6a0)
- Hirai, R., Sawai, H., & Yamada, S. 2014, *ApJ*, 792, 66, doi: [10.1088/0004-637X/792/1/66](https://doi.org/10.1088/0004-637X/792/1/66)
- Ho, W. C. G., & Andersson, N. 2017, *MNRAS*, 464, L65, doi: [10.1093/mnrasl/slwl186](https://doi.org/10.1093/mnrasl/slwl186)
- Hobbs, G., Lorimer, D. R., Lyne, A. G., & Kramer, M. 2005, *MNRAS*, 360, 974, doi: [10.1111/j.1365-2966.2005.09087.x](https://doi.org/10.1111/j.1365-2966.2005.09087.x)
- Hulleman, F., van Kerkwijk, M. H., & Kulkarni, S. R. 2004, *A&A*, 416, 1037, doi: [10.1051/0004-6361:20031756](https://doi.org/10.1051/0004-6361:20031756)
- Hunter, J. D. 2007, *Computing in Science & Engineering*, 9, 90, doi: [10.1109/MCSE.2007.55](https://doi.org/10.1109/MCSE.2007.55)
- Hurley-Walker, N., Zhang, X., Bahramian, A., et al. 2022, *Nature*, 601, 526, doi: [10.1038/s41586-021-04272-x](https://doi.org/10.1038/s41586-021-04272-x)
- Hurley-Walker, N., Rea, N., McSweeney, S. J., et al. 2023, *Nature*, 619, 487, doi: [10.1038/s41586-023-06202-5](https://doi.org/10.1038/s41586-023-06202-5)
- Hurley-Walker, N., McSweeney, S. J., Bahramian, A., et al. 2024, *ApJL*, 976, L21, doi: [10.3847/2041-8213/ad890e](https://doi.org/10.3847/2041-8213/ad890e)
- Ichikawa, S., & Osaki, Y. 1992, *PASJ*, 44, 15
- Iglesias, C. A., & Rogers, F. J. 1996, *ApJ*, 464, 943, doi: [10.1086/177381](https://doi.org/10.1086/177381)
- Igoshev, A. P., & Popov, S. B. 2018, *Research Notes of the American Astronomical Society*, 2, 171, doi: [10.3847/2515-5172/aae207](https://doi.org/10.3847/2515-5172/aae207)
- Inutsuka, S.-i., & Sano, T. 2005, *ApJL*, 628, L155, doi: [10.1086/432796](https://doi.org/10.1086/432796)
- Israel, G. L., Burgay, M., Rea, N., et al. 2021, *ApJ*, 907, 7, doi: [10.3847/1538-4357/abca95](https://doi.org/10.3847/1538-4357/abca95)
- Janka, H.-T., Wongwathanarat, A., & Kramer, M. 2022, *ApJ*, 926, 9, doi: [10.3847/1538-4357/ac403c](https://doi.org/10.3847/1538-4357/ac403c)
- Kaplan, D. L., Chakrabarty, D., Wang, Z., & Wachter, S. 2009, *ApJ*, 700, 149, doi: [10.1088/0004-637X/700/1/149](https://doi.org/10.1088/0004-637X/700/1/149)
- Kasen, D. 2010, *The Astrophysical Journal*, 708, 1025, doi: [10.1088/0004-637X/708/2/1025](https://doi.org/10.1088/0004-637X/708/2/1025)
- Kaspi, V. M., & Beloborodov, A. M. 2017, *ARA&A*, 55, 261, doi: [10.1146/annurev-astro-081915-023329](https://doi.org/10.1146/annurev-astro-081915-023329)
- Katz, J. I. 2022, *Ap&SS*, 367, 108, doi: [10.1007/s10509-022-04146-2](https://doi.org/10.1007/s10509-022-04146-2)
- Keane, E. F., & Kramer, M. 2008, *MNRAS*, 391, 2009, doi: [10.1111/j.1365-2966.2008.14045.x](https://doi.org/10.1111/j.1365-2966.2008.14045.x)
- Kou, F. F., Tong, H., Xu, R. X., & Zhou, X. 2019, *ApJ*, 876, 131, doi: [10.3847/1538-4357/ab17da](https://doi.org/10.3847/1538-4357/ab17da)
- Langer, N. 2012, *ARA&A*, 50, 107, doi: [10.1146/annurev-astro-081811-125534](https://doi.org/10.1146/annurev-astro-081811-125534)
- Lazarus, P., Brazier, A., Hessels, J. W. T., et al. 2015, *ApJ*, 812, 81, doi: [10.1088/0004-637X/812/1/81](https://doi.org/10.1088/0004-637X/812/1/81)
- Levin, L., Bailes, M., Bates, S., et al. 2010, *ApJL*, 721, L33, doi: [10.1088/2041-8205/721/1/L33](https://doi.org/10.1088/2041-8205/721/1/L33)
- Li, D., Yuan, M., Wu, L., et al. 2024, *arXiv e-prints*, arXiv:2411.15739, doi: [10.48550/arXiv.2411.15739](https://doi.org/10.48550/arXiv.2411.15739)
- Li, W., Leaman, J., Chornock, R., et al. 2011, *MNRAS*, 412, 1441, doi: [10.1111/j.1365-2966.2011.18160.x](https://doi.org/10.1111/j.1365-2966.2011.18160.x)
- Lin, D. N. C., Woosley, S. E., & Bodenheimer, P. H. 1991, *Nature*, 353, 827, doi: [10.1038/353827a0](https://doi.org/10.1038/353827a0)

- Liu, Z.-W., Tauris, T. M., Röpké, F. K., et al. 2015, *A&A*, 584, A11, doi: [10.1051/0004-6361/201526757](https://doi.org/10.1051/0004-6361/201526757)
- Loeb, A., & Maoz, D. 2022, *Research Notes of the American Astronomical Society*, 6, 27, doi: [10.3847/2515-5172/ac52f1](https://doi.org/10.3847/2515-5172/ac52f1)
- Lu, W., Beniamini, P., & Kumar, P. 2022, *MNRAS*, 510, 1867, doi: [10.1093/mnras/stab3500](https://doi.org/10.1093/mnras/stab3500)
- Lyman, J. D., Bersier, D., James, P. A., et al. 2016, *MNRAS*, 457, 328, doi: [10.1093/mnras/stv2983](https://doi.org/10.1093/mnras/stv2983)
- Manchester, R. N., Hobbs, G. B., Teoh, A., & Hobbs, M. 2005, *AJ*, 129, 1993, doi: [10.1086/428488](https://doi.org/10.1086/428488)
- Mao, Y.-H., Li, X.-D., Lai, D., Deng, Z.-L., & Yang, H.-R. 2025, A binary origin of ultra-long period radio pulsars, <https://arxiv.org/abs/2507.00946>
- Marcote, B., Marsh, T. R., Stanway, E. R., Paragi, Z., & Blanchard, J. M. 2017, *A&A*, 601, L7, doi: [10.1051/0004-6361/201730948](https://doi.org/10.1051/0004-6361/201730948)
- Marsh, T. R., Gänsicke, B. T., Hümmerich, S., et al. 2016, *Nature*, 537, 374, doi: [10.1038/nature18620](https://doi.org/10.1038/nature18620)
- Metzger, B. D., Beniamini, P., & Giannios, D. 2018, *ApJ*, 857, 95, doi: [10.3847/1538-4357/aab70c](https://doi.org/10.3847/1538-4357/aab70c)
- Michel, F. C. 1988, *Nature*, 333, 644, doi: [10.1038/333644a0](https://doi.org/10.1038/333644a0)
- Noutsos, A., Schnitzeler, D. H. F. M., Keane, E. F., Kramer, M., & Johnston, S. 2013, *MNRAS*, 430, 2281, doi: [10.1093/mnras/stt047](https://doi.org/10.1093/mnras/stt047)
- Offner, S. S. R., Moe, M., Kratter, K. M., et al. 2023, in *Astronomical Society of the Pacific Conference Series*, Vol. 534, *Protostars and Planets VII*, ed. S. Inutsuka, Y. Aikawa, T. Muto, K. Tomida, & M. Tamura, 275, doi: [10.48550/arXiv.2203.10066](https://doi.org/10.48550/arXiv.2203.10066)
- Ogata, M., Hirai, R., & Hijikawa, K. 2021, *MNRAS*, 505, 2485, doi: [10.1093/mnras/stab1439](https://doi.org/10.1093/mnras/stab1439)
- Olausen, S. A., & Kaspi, V. M. 2014, *ApJS*, 212, 6, doi: [10.1088/0067-0049/212/1/6](https://doi.org/10.1088/0067-0049/212/1/6)
- Owen, J. E., Clarke, C. J., & Ercolano, B. 2012, *MNRAS*, 422, 1880, doi: [10.1111/j.1365-2966.2011.20337.x](https://doi.org/10.1111/j.1365-2966.2011.20337.x)
- Page, D., Lattimer, J. M., Prakash, M., & Steiner, A. W. 2004, *ApJS*, 155, 623, doi: [10.1086/424844](https://doi.org/10.1086/424844)
- Parfrey, K., Spitkovsky, A., & Beloborodov, A. M. 2016, *ApJ*, 822, 33, doi: [10.3847/0004-637X/822/1/33](https://doi.org/10.3847/0004-637X/822/1/33)
- Pelisoli, I., Marsh, T. R., Buckley, D. A. H., et al. 2023, *Nature Astronomy*, 7, 931, doi: [10.1038/s41550-023-01995-x](https://doi.org/10.1038/s41550-023-01995-x)
- Perna, R., Duffell, P., Cantiello, M., & MacFadyen, A. I. 2014, *ApJ*, 781, 119, doi: [10.1088/0004-637X/781/2/119](https://doi.org/10.1088/0004-637X/781/2/119)
- Perna, R., Hernquist, L., & Narayan, R. 2000, *ApJ*, 541, 344, doi: [10.1086/309404](https://doi.org/10.1086/309404)
- Phinney, E. S., & Hansen, B. M. S. 1993, in *Astronomical Society of the Pacific Conference Series*, Vol. 36, *Planets Around Pulsars*, ed. J. A. Phillips, S. E. Thorsett, & S. R. Kulkarni, 371–390
- Piro, A. L., & Ott, C. D. 2011, *ApJ*, 736, 108, doi: [10.1088/0004-637X/736/2/108](https://doi.org/10.1088/0004-637X/736/2/108)
- Podsiadlowski, P., Joss, P. C., & Hsu, J. J. L. 1992, *ApJ*, 391, 246, doi: [10.1086/171341](https://doi.org/10.1086/171341)
- Pons, J. A., & Geppert, U. 2007, *A&A*, 470, 303, doi: [10.1051/0004-6361:20077456](https://doi.org/10.1051/0004-6361:20077456)
- Popov, S. B., & Turolla, R. 2012, *Ap&SS*, 341, 457, doi: [10.1007/s10509-012-1100-z](https://doi.org/10.1007/s10509-012-1100-z)
- Prentice, S. J., Ashall, C., James, P. A., et al. 2018, *Monthly Notices of the Royal Astronomical Society*, 485, 1559–1578, doi: [10.1093/mnras/sty3399](https://doi.org/10.1093/mnras/sty3399)
- Prentice, S. J., Ashall, C., James, P. A., et al. 2019, *MNRAS*, 485, 1559, doi: [10.1093/mnras/sty3399](https://doi.org/10.1093/mnras/sty3399)
- Qu, Y., & Zhang, B. 2024, *arXiv e-prints*, arXiv:2409.05978, doi: [10.48550/arXiv.2409.05978](https://doi.org/10.48550/arXiv.2409.05978)
- Raghavan, D., McAlister, H. A., Henry, T. J., et al. 2010, *ApJS*, 190, 1, doi: [10.1088/0067-0049/190/1/1](https://doi.org/10.1088/0067-0049/190/1/1)
- Ragosta, F., Illiano, G., Simongini, A., et al. 2025, *arXiv e-prints*, arXiv:2503.15977, doi: [10.48550/arXiv.2503.15977](https://doi.org/10.48550/arXiv.2503.15977)
- Rodriguez, A. C. 2025, *arXiv e-prints*, arXiv:2501.03315, doi: [10.48550/arXiv.2501.03315](https://doi.org/10.48550/arXiv.2501.03315)
- Ronchi, M., Rea, N., Graber, V., & Hurley-Walker, N. 2022, *ApJ*, 934, 184, doi: [10.3847/1538-4357/ac7cec](https://doi.org/10.3847/1538-4357/ac7cec)
- Sana, H., de Mink, S. E., de Koter, A., et al. 2012, *Science*, 337, 444, doi: [10.1126/science.1223344](https://doi.org/10.1126/science.1223344)
- Sana, H., de Koter, A., de Mink, S. E., et al. 2013, *A&A*, 550, A107, doi: [10.1051/0004-6361/201219621](https://doi.org/10.1051/0004-6361/201219621)
- Shakura, N. I., & Sunyaev, R. A. 1973, *A&A*, 24, 337
- Shapiro, S. L., & Teukolsky, S. A. 1983, *Black holes, white dwarfs and neutron stars. The physics of compact objects*, doi: [10.1002/9783527617661](https://doi.org/10.1002/9783527617661)
- Shen, R.-F., & Matzner, C. D. 2014, *ApJ*, 784, 87, doi: [10.1088/0004-637X/784/2/87](https://doi.org/10.1088/0004-637X/784/2/87)
- Shivvers, I., Modjaz, M., Zheng, W., et al. 2017, *PASP*, 129, 054201, doi: [10.1088/1538-3873/aa54a6](https://doi.org/10.1088/1538-3873/aa54a6)
- Smartt, S. J. 2015, *PASA*, 32, e016, doi: [10.1017/pasa.2015.17](https://doi.org/10.1017/pasa.2015.17)
- Smith, N., Li, W., Filippenko, A. V., & Chornock, R. 2011, *MNRAS*, 412, 1522, doi: [10.1111/j.1365-2966.2011.17229.x](https://doi.org/10.1111/j.1365-2966.2011.17229.x)
- Stella, L., White, N. E., & Rosner, R. 1986, *ApJ*, 308, 669, doi: [10.1086/164538](https://doi.org/10.1086/164538)
- Stone, J. M., Tomida, K., White, C. J., & Felker, K. G. 2020, *ApJS*, 249, 4, doi: [10.3847/1538-4365/ab929b](https://doi.org/10.3847/1538-4365/ab929b)

- Taddia, F., Sollerman, J., Leloudas, G., et al. 2015, *A&A*, 574, A60, doi: [10.1051/0004-6361/201423915](https://doi.org/10.1051/0004-6361/201423915)
- Taddia, F., Stritzinger, M. D., Bersten, M., et al. 2018, *A&A*, 609, A136, doi: [10.1051/0004-6361/201730844](https://doi.org/10.1051/0004-6361/201730844)
- Tan, C. M., Bassa, C. G., Cooper, S., et al. 2018, *ApJ*, 866, 54, doi: [10.3847/1538-4357/aade88](https://doi.org/10.3847/1538-4357/aade88)
- Tendulkar, S. P., Kaspi, V. M., Archibald, R. F., & Scholz, P. 2017, *ApJ*, 841, 11, doi: [10.3847/1538-4357/aa6d0c](https://doi.org/10.3847/1538-4357/aa6d0c)
- Tomida, K., & Stone, J. M. 2023, *ApJS*, 266, 7, doi: [10.3847/1538-4365/acc2c0](https://doi.org/10.3847/1538-4365/acc2c0)
- Tong, H. 2023, *ApJ*, 943, 3, doi: [10.3847/1538-4357/aca7fa](https://doi.org/10.3847/1538-4357/aca7fa)
- Tong, H., Wang, W., Liu, X. W., & Xu, R. X. 2016, *ApJ*, 833, 265, doi: [10.3847/1538-4357/833/2/265](https://doi.org/10.3847/1538-4357/833/2/265)
- Toyouchi, D., Hotokezaka, K., Inayoshi, K., & Kuiper, R. 2024, *MNRAS*, 532, 4826, doi: [10.1093/mnras/stae1798](https://doi.org/10.1093/mnras/stae1798)
- Ugliano, M., Janka, H.-T., Marek, A., & Arcones, A. 2012, *ApJ*, 757, 69, doi: [10.1088/0004-637X/757/1/69](https://doi.org/10.1088/0004-637X/757/1/69)
- van Heerden, E., Karastergiou, A., & Roberts, S. J. 2017, *MNRAS*, 467, 1661, doi: [10.1093/mnras/stw3068](https://doi.org/10.1093/mnras/stw3068)
- Virtanen, P., Gommers, R., Oliphant, T. E., et al. 2020, *Nature Methods*, 17, 261, doi: [10.1038/s41592-019-0686-2](https://doi.org/10.1038/s41592-019-0686-2)
- Vishniac, E. T., & Wheeler, J. C. 1996, *ApJ*, 471, 921, doi: [10.1086/178019](https://doi.org/10.1086/178019)
- Wang, Z., Chakrabarty, D., & Kaplan, D. L. 2006, *Nature*, 440, 772, doi: [10.1038/nature04669](https://doi.org/10.1038/nature04669)
- Wang, Z., Rea, N., Bao, T., et al. 2024, arXiv e-prints, arXiv:2411.16606, doi: [10.48550/arXiv.2411.16606](https://doi.org/10.48550/arXiv.2411.16606)
- Wolszczan, A., & Frail, D. A. 1992, *Nature*, 355, 145, doi: [10.1038/355145a0](https://doi.org/10.1038/355145a0)
- Wong, T. L. S., White, C., & Bildsten, L. 2024, Shocking and Mass Loss of Compact Donor Stars in Type Ia Supernovae, <https://arxiv.org/abs/2408.00125>
- Woosley, S. E., Sukhbold, T., & Kasen, D. N. 2021, *ApJ*, 913, 145, doi: [10.3847/1538-4357/abf3be](https://doi.org/10.3847/1538-4357/abf3be)
- Yang, H.-R., Li, X.-D., Gao, S.-J., & Xu, K. 2024, *ApJ*, 976, 77, doi: [10.3847/1538-4357/ad83d4](https://doi.org/10.3847/1538-4357/ad83d4)
- Yoon, S. C., Gräfener, G., Vink, J. S., Kozyreva, A., & Izzard, R. G. 2012, *A&A*, 544, L11, doi: [10.1051/0004-6361/201219790](https://doi.org/10.1051/0004-6361/201219790)
- Yuan, F., Bu, D., & Wu, M. 2012, *ApJ*, 761, 130, doi: [10.1088/0004-637X/761/2/130](https://doi.org/10.1088/0004-637X/761/2/130)
- Zhang, B., Harding, A. K., & Muslimov, A. G. 2000, *ApJL*, 531, L135, doi: [10.1086/312542](https://doi.org/10.1086/312542)
- Zhou, X., Huang, H.-T., Cheng, Q., & Zheng, X.-P. 2024, *MNRAS*, 530, 1636, doi: [10.1093/mnras/stae954](https://doi.org/10.1093/mnras/stae954)
- Zhu, W., Xu, H., Zhou, D., et al. 2023, *Science Advances*, 9, eadf6198, doi: [10.1126/sciadv.adf6198](https://doi.org/10.1126/sciadv.adf6198)